The 3-D Unconditionally Stable Multisymplectic FDTD Method for the Computational Electromagnetic Simulation

Zhipeng Chen, Linqing Li, Chao Yang, Wei E. I. Sha, *Senior Member, IEEE*, Yingsong Li, *Senior Member, IEEE*, Zhixiang Huang, *Senior Member, IEEE*, Xianliang Wu, Atef Z. Elsherbeni, *Life Fellow, IEEE*, and Kaikun Niu, *Member, IEEE*

***Abstract*—This research presents a 3-D unconditionally stable multisymplectic finite-difference time-domain (MS-FDTD) method, marking a significant advance in computational electromagnetics. For the first time, the locally one-dimensional (LOD)-FDTD method is applied to the multisymplectic Preissman scheme of Maxwell's equations. A new grid arrangement for electric and magnetic fields is designed to meet MS-FDTD discretization requirements, differing fundamentally from the traditional Yee grid. We have derived the detailed equations and techniques for implementing various boundary conditions in the proposed method. An in-depth analysis of numerical dispersion has been conducted, demonstrating the method's superior characteristics in this regard compared to traditional finite-difference time-domain (FDTD) methods. Additionally, the unconditional stability of our method has been thoroughly confirmed. Comprehensive simulations, including cavity resonances, bioelectromagnetic problems, and on-chip applications, validate its accuracy, efficiency, and long-term stability. This work integrates multisymplectic theory, originating from mathematics, into computational electromagnetics, providing a novel framework for numerical algorithms.**

***Index Terms*—Finite difference time domain (FDTD), multisymplectic, numerical dispersion, stability analysis.**

I. Introduction

THE finite-difference time-domain (FDTD) method is one of the most widely used algorithms in computational electromagnetics, valued for its simplicity and high computational efficiency. It is particularly suited for solving transient electromagnetic problems and modeling complex, inhomogeneous structures within the computational domain. Applications include electromagnetic wave propagation [1], scattering analysis [2], antenna design, and photonic device simulation [3].

Despite these advantages, the FDTD method has significant limitations that affect its accuracy and stability. Key challenges include numerical instability, numerical dispersion, and cumulative error in long-duration simulations, as well as restrictions on computational accuracy. Stability requires adherence to the Courant–Friedrichs–Lewy (CFL) condition, which imposes strict limits on the time step relative to spatial resolution. High-resolution problems often demand extremely small time steps, increasing memory and computational costs. To address this, several advanced FDTD techniques with unconditional and conditionally stable properties have been developed to alleviate the CFL constraint [4]. These include the locally one-dimensional FDTD (LOD-FDTD) scheme [5], [6], [7], [8], the alternating direction implicit FDTD (ADI-FDTD) scheme [9], [10], [11], the hybrid implicit–explicit FDTD (HIE-FDTD) scheme [12], [13], [14], [15], [16], and the weakly conditionally stable FDTD (WCS-FDTD) method [17], [18]. However, the tradeoff for obtaining more relaxed stability conditions with the above methods is a reduction in numerical dispersion accuracy. As a result, researchers have proposed the higher order FDTD algorithm [19], [20] and the artificial anisotropic FDTD algorithm [21], [22] to improve numerical accuracy.

However, these methods still cannot address the long-term stability issue. In the early 1980s, Feng [23] and Ruth [24] independently introduced the symplectic algorithm, a numerical integration method highly effective for Hamiltonian systems due to its superior numerical prediction and tracking capabilities. It has broad applications across scientific, technical, and engineering fields. The structure-preserving nature of the symplectic algorithm has become a cornerstone in modern computational mathematics, driving research in scientific computing. The source-free Maxwell's equations with constant scalar parameters possess a symplectic structure, enabling compatibility with symplectic algorithms. Combined with the FDTD method, they form the symplectic FDTD (S-FDTD) algorithm [25], [26], [27], [28], [29], which provides significant advantages over standard methods in terms of numerical stability and long-term computational performance.

Received 29 November 2024; revised 26 June 2025; accepted 23 September 2025. Date of publication 8 October 2025; date of current version 18 December 2025. This work was supported in part by the National Natural Science Foundation of China under Grant 62101002, Grant U22A2017, and Grant U23A20290; in part by the National Natural Science Foundation of China through the Key Program under Grant 62531001; in part by the Natural Science Foundation of Anhui Province under Grant 2508085Y037; in part by Anhui Province Science and Technology Innovation Tackle Plan Project under Grant 202423k09020033; and in part by the State Key Laboratory of Radio Frequency Heterogeneous Integration through the Open Scientific Research Program under Grant KF2024001. *(Corresponding author: Kaikun Niu.)*

Zhipeng Chen, Linqing Li, Yingsong Li, Zhixiang Huang, Xianliang Wu, and Kaikun Niu are with the State Key Laboratory of Optoelectronic Information Acquisition and Protection Technology, Information Materials and Intelligent Sensing Laboratory of Anhui Province, Anhui University, Hefei 230601, China (e-mail: kkniu@ahu.edu.cn).

Chao Yang is with the National Key Laboratory of Intense Pulsed Radiation Simulation and Effect, Xi'an 710024, China.

Wei E. I. Sha is with the Innovative Institute of Electromagnetic Information and Electronic Integration, College of Information Science and Electronic Engineering, Zhejiang University, Hangzhou 310058, China.

Atef Z. Elsherbeni is with the Department of Electrical and Computer Engineering, Colorado School of Mines, Golden, CO 80401 USA.

Digital Object Identifier 10.1109/TAP.2025.3617119

Maxwell's equations also exhibit a multisymplectic structure, an extension of the symplectic formulation for Hamiltonian systems, as proposed by Bridges and Reich [30] and Marsden et al. [31]. The multisymplectic scheme differs from the symplectic scheme by adhering not only to global energy conservation but also to local conservation laws, known as multisymplectic conservation laws (MSCLs) [32]. MSCL ensures that the infinite-dimensional Hamiltonian system follows both a local energy conservation law and a momentum conservation law [33], maintaining the symplectic structure in both space and time. The benefits of the multisymplectic scheme have been successfully demonstrated in numerous equations, including the Korteweg–de Vries equation [34], the Kadomtsev–Petviashvili equation [35], the Zakharov–Kuznetsov equation [36], and the nonlinear Schrödinger equation [37].

Previous research has primarily been dedicated to the mathematical analysis and theoretical exploration of various multisymplectic schemes for Maxwell's equations. Notable among these are the multisymplectic Preissman scheme, the multisymplectic Euler-box scheme [38], the multisymplectic wavelet collocation scheme [39], and splitting multisymplectic integrators [40]. Mathematical analyses, including numerical dispersion studies, have verified that these schemes are significantly superior to other methods regarding long-term computation and numerical stability [38], [39], [40], [41], [42]. For the numerical example, the Preissman and Euler-box schemes were applied to 2-D periodic boundary conditions, while the splitting multisymplectic integrator used symplectic Runge–Kutta methods for discretization, with perfect electric conductor (PEC) boundary conditions. However, these schemes face challenges with discontinuous boundary conditions.

To the best of the author's knowledge, existing studies primarily provide 2-D numerical examples, and the setting of structural and material parameters is devoid of practical physical significance and consists of unitless numerical values. This approach limits the ability of these models to accurately reflect real-world physical conditions. At the same time, comprehensive physical boundary conditions and detailed 3-D electromagnetic field mesh distributions have not been researched. Overall, no prior literature has specifically addressed the application of multisymplectic schemes in computational electromagnetics to simulate practical 3-D engineering problems. Thus, bridging the gap between mathematical theory and numerical algorithms based on multisymplectic schemes in electromagnetics is essential for advancing realistic applications.

This article introduces, for the first time, a multisymplectic FDTD (MS-FDTD) method for solving Maxwell's equations. The main innovations of this article are summarized as follows.

1) We employ the LOD method to discretize the multisymplectic Preissman scheme for Maxwell's equations, resulting in the LOD multisymplectic Preissman scheme, which achieves unconditional stability. Using the symplectic midpoint scheme in both the time and spatial directions, we derive the 3-D implicit iterative equations for electromagnetic fields, ensuring the stability and accuracy of numerical solutions.
2) Numerical stability analyses based on the Fourier method are conducted, confirming the unconditional stability of the proposed MS-FDTD method. Additionally, numerical dispersion analyses show that the numerical error of the proposed method is superior to that of the conventional FDTD method.
3) A novel grid configuration for the magnetic and electric fields is developed to meet the discretization requirements of the MS-FDTD Preissman method, differing entirely from the traditional Yee grid used in FDTD methods.
4) Given the distinct grid structure, iterative methods, and matrix-solving techniques of the MS-FDTD method, we propose specific boundary techniques, including PEC, periodic boundary, and excitation source techniques.
5) Several numerical examples are provided, ranging from one to 3-D cases, involving resonant cavities, bioelectromagnetic applications, and onboard chip. These examples demonstrate the accuracy, efficiency, and stability of the proposed MS-FDTD method compared to the conventional FDTD approach.

The organization of this article is as follows. In Section II, we derive the complete formulation of the MS-FDTD method and utilize a splitting method to decompose it, obtaining iterative formulas suitable for straightforward computation. Section III conducts stability analyses of both the nonsplit and split forms of the MS-FDTD method, deriving their dispersion relations. Section IV presents numerical examples in three dimensions to validate the performance of the proposed MS-FDTD method. Finally, Section V provides the conclusions.

II. Formulation

The set of Maxwell's equations in each isotropic, homogeneous, nondissipative medium is

$$\nabla \times \mathbf{E} = -\mu \frac{\partial \mathbf{H}}{\partial t} \tag{1}$$

$$\nabla \times \mathbf{H} = \varepsilon \frac{\partial \mathbf{E}}{\partial t} \tag{2}$$

$$\nabla \cdot \mathbf{B} = 0 \tag{3}$$

$$\nabla \cdot \mathbf{E} = 0. \tag{4}$$

The Hamiltonian equations for a multisymplectic scheme with m spatial dimensions are

$$\mathbf{M}Z_t + \mathbf{K_1}Z_1 + \mathbf{K_2}Z_2 + \mathbf{K_3}Z_3 = \nabla_Z S\,(\mathbf{z}) \tag{5}$$

where

$$\mathbf{M} = \begin{bmatrix} 0 & 0 & 0 & 0 & 0 & 0 \\ 0 & 0 & 0 & 0 & 0 & 0 \\ 0 & 0 & 0 & 0 & -I & 0 \\ 0 & 0 & 0 & 0 & 0 & -I \\ 0 & 0 & I & 0 & 0 & 0 \\ 0 & 0 & 0 & I & 0 & 0 \end{bmatrix}$$

$$\mathbf{K_1} = \begin{bmatrix} 0 & 0 & 0 & \frac{1}{2}C_1 & 0 & 0 \\ 0 & 0 & -\frac{1}{2}C_1 & 0 & 0 & 0 \\ 0 & \frac{1}{2}C_1 & 0 & 0 & 0 & 0 \\ -\frac{1}{2}C_1 & 0 & 0 & 0 & 0 & 0 \\ 0 & 0 & 0 & 0 & 0 & 0 \\ 0 & 0 & 0 & 0 & 0 & 0 \end{bmatrix}$$

$$\mathbf{K_2}=\begin{bmatrix} 0 & 0 & 0 & \frac{1}{2}C_2 & 0 & 0\\ 0 & 0 & \frac{1}{2}C_2 & 0 & 0 & 0\\ 0 & -\frac{1}{2}C_2 & 0 & 0 & 0 & 0\\ \frac{1}{2}C_2 & 0 & 0 & 0 & 0 & 0\\ 0 & 0 & 0 & 0 & 0 & 0\\ 0 & 0 & 0 & 0 & 0 & 0 \end{bmatrix}$$

$$\mathbf{K_3}=\begin{bmatrix} 0 & 0 & 0 & \frac{1}{2}C_3 & 0 & 0\\ 0 & 0 & -\frac{1}{2}C_3 & 0 & 0 & 0\\ 0 & \frac{1}{2}C_3 & 0 & 0 & 0 & 0\\ -\frac{1}{2}C_3 & 0 & 0 & 0 & 0 & 0\\ 0 & 0 & 0 & 0 & 0 & 0\\ 0 & 0 & 0 & 0 & 0 & 0 \end{bmatrix}$$

$$\mathbf{C_1}=\begin{bmatrix} 0 & 0 & 0\\ 0 & 0 & -1\\ 0 & 1 & 0 \end{bmatrix},\quad \mathbf{C_2}=\begin{bmatrix} 0 & 0 & 1\\ 0 & 0 & 0\\ -1 & 0 & 0 \end{bmatrix}$$

$$\mathbf{C_3}=\begin{bmatrix} 0 & -1 & 0\\ 1 & 0 & 0\\ 0 & 0 & 0 \end{bmatrix}$$

in which $\boldsymbol{I}$ is the identity element belonging to $\boldsymbol{R}^{3\times 3}$. $\mathbf{M}$ and $\mathbf{K}$ are antisymmetric matrices and $S(\mathbf{z})$ is a smoothing function that has been made a Hamiltonian or energy generalization. Bridges and Reich defined the numerical scheme that maintains the discrete MSCL as the multisymplectic scheme. Maintaining the discrete MSCL means that the corresponding multisymplectic scheme satisfies local energy conservation and local momentum conservation. Discretize (5) using the symplectic midpoint scheme to obtain the Preissman scheme

$$\begin{aligned}&\nabla_z S\left(Z^{n+\frac{1}{2}}_{x+\frac{1}{2},y+\frac{1}{2},z+\frac{1}{2}}\right)\\ &\quad=\mathbf{M}\frac{Z^{n+1}_{i+\frac{1}{2},j+\frac{1}{2},k+\frac{1}{2}}-Z^{n}_{i+\frac{1}{2},j+\frac{1}{2},k+\frac{1}{2}}}{\Delta t}\\ &\qquad+\mathbf{K_1}\frac{Z^{n+\frac{1}{2}}_{i+1,j+\frac{1}{2},k+\frac{1}{2}}-Z^{n+\frac{1}{2}}_{i,j+\frac{1}{2},k+\frac{1}{2}}}{\Delta x}\\ &\qquad+\mathbf{K_2}\frac{Z^{n+\frac{1}{2}}_{i+\frac{1}{2},j+1,k+\frac{1}{2}}-Z^{n+\frac{1}{2}}_{i+\frac{1}{2},j,k+\frac{1}{2}}}{\Delta y}\\ &\qquad+\mathbf{K_3}\frac{Z^{n+\frac{1}{2}}_{i+\frac{1}{2},j+\frac{1}{2},k+1}-Z^{n+\frac{1}{2}}_{i+\frac{1}{2},j+\frac{1}{2},k}}{\Delta z}.\end{aligned}\tag{6}$$

The Preissman scheme in (6) is multisymplectic and satisfies the discrete MSCL. Substitution of Maxwell's system of equations into (6) yields the multisymplectic Preissman scheme of Maxwell's system of equations

$$\begin{aligned}&E^{n+1}_{x_{i+\frac{1}{2},j+\frac{1}{2},k+\frac{1}{2}}}-\frac{\Delta t}{2\varepsilon}\left(\delta_y H^{n+1}_{z_{i+\frac{1}{2},j,k+\frac{1}{2}}}-\delta_z H^{n+1}_{y_{i+\frac{1}{2},j+\frac{1}{2},k}}\right)\\ &\quad=E^{n}_{x_{i+\frac{1}{2},j+\frac{1}{2},k+\frac{1}{2}}}+\frac{\Delta t}{2\varepsilon}\left(\delta_y H^{n}_{z_{i+\frac{1}{2},j,k+\frac{1}{2}}}-\delta_z H^{n}_{y_{i+\frac{1}{2},j+\frac{1}{2},k}}\right)\\ &E^{n+1}_{y_{i+\frac{1}{2},j+\frac{1}{2},k+\frac{1}{2}}}-\frac{\Delta t}{2\varepsilon}\left(\delta_z H^{n+1}_{x_{i+\frac{1}{2},j+\frac{1}{2},k}}-\delta_x H^{n+1}_{z_{i,j+\frac{1}{2},k+\frac{1}{2}}}\right)\\ &\quad=E^{n}_{y_{i+\frac{1}{2},j+\frac{1}{2},k+\frac{1}{2}}}+\frac{\Delta t}{2\varepsilon}\left(\delta_z H^{n}_{x_{i+\frac{1}{2},j+\frac{1}{2},k}}-\delta_x H^{n}_{z_{i,j+\frac{1}{2},k+\frac{1}{2}}}\right)\end{aligned}\tag{7}$$

$$\begin{aligned}&E^{n+1}_{z_{i+\frac{1}{2},j+\frac{1}{2},k+\frac{1}{2}}}-\frac{\Delta t}{2\varepsilon}\left(\delta_x H^{n+1}_{y_{i,j+\frac{1}{2},k+\frac{1}{2}}}-\delta_y H^{n+1}_{x_{i+\frac{1}{2},j,k+\frac{1}{2}}}\right)\\ &\quad=E^{n}_{z_{i+\frac{1}{2},j+\frac{1}{2},k+\frac{1}{2}}}+\frac{\Delta t}{2\varepsilon}\left(\delta_x H^{n}_{y_{i,j+\frac{1}{2},k+\frac{1}{2}}}-\delta_y H^{n}_{x_{i+\frac{1}{2},j,k+\frac{1}{2}}}\right)\end{aligned}\tag{8}$$

$$\begin{aligned}&H^{n+1}_{x_{i+\frac{1}{2},j+\frac{1}{2},k+\frac{1}{2}}}-\frac{\Delta t}{2\mu}\left(\delta_z E^{n+1}_{y_{i+\frac{1}{2},j+\frac{1}{2},k}}-\delta_y E^{n+1}_{z_{i+\frac{1}{2},j,k+\frac{1}{2}}}\right)\\ &\quad=H^{n}_{x_{i+\frac{1}{2},j+\frac{1}{2},k+\frac{1}{2}}}+\frac{\Delta t}{2\mu}\left(\delta_z E^{n}_{y_{i+\frac{1}{2},j+\frac{1}{2},k}}-\delta_y E^{n}_{z_{i+\frac{1}{2},j,k+\frac{1}{2}}}\right)\end{aligned}\tag{9}$$

$$\begin{aligned}&H^{n+1}_{y_{i+\frac{1}{2},j+\frac{1}{2},k+\frac{1}{2}}}-\frac{\Delta t}{2\mu}\left(\delta_x E^{n+1}_{z_{i,j+\frac{1}{2},k+\frac{1}{2}}}-\delta_z E^{n+1}_{x_{i+\frac{1}{2},j+\frac{1}{2},k}}\right)\\ &\quad=H^{n}_{y_{i+\frac{1}{2},j+\frac{1}{2},k+\frac{1}{2}}}+\frac{\Delta t}{2\mu}\left(\delta_x E^{n}_{z_{i,j+\frac{1}{2},k+\frac{1}{2}}}-\delta_z E^{n}_{x_{i+\frac{1}{2},j+\frac{1}{2},k}}\right)\end{aligned}\tag{10}$$

$$\begin{aligned}&H^{n+1}_{z_{i+\frac{1}{2},j+\frac{1}{2},k+\frac{1}{2}}}-\frac{\Delta t}{2\mu}\left(\delta_y E^{n+1}_{x_{i+\frac{1}{2},j,k+\frac{1}{2}}}-\delta_x E^{n+1}_{y_{i,j+\frac{1}{2},k+\frac{1}{2}}}\right)\\ &\quad=H^{n}_{z_{i+\frac{1}{2},j+\frac{1}{2},k+\frac{1}{2}}}+\frac{\Delta t}{2\mu}\left(\delta_y E^{n}_{x_{i+\frac{1}{2},j,k+\frac{1}{2}}}-\delta_x E^{n}_{y_{i,j+\frac{1}{2},k+\frac{1}{2}}}\right).\end{aligned}\tag{11}$$

The symplectic midpoint-discrete operator is as follows:

$$\delta_t Z^n_{i+\frac{1}{2}}=\frac{1}{\Delta t}\left(Z^{n+1}_{i+\frac{1}{2}}-Z^{n}_{i+\frac{1}{2}}\right)\tag{12}$$

$$\delta_x Z^{n+\frac{1}{2}}_{i}=\frac{1}{\Delta x}\left(Z^{n+\frac{1}{2}}_{i+1}-Z^{n+\frac{1}{2}}_{i}\right)\tag{13}$$

$$Z^{n+\frac{1}{2}}_{i}=\frac{1}{2}\left(Z^{n+1}_{i}+Z^{n}_{i}\right)\tag{14}$$

$$Z^{n}_{i+\frac{1}{2}}=\frac{1}{2}\left(Z^{n}_{i+1}+Z^{n}_{i}\right)\tag{15}$$

$$Z^{n+\frac{1}{2}}_{i+\frac{1}{2}}=\frac{1}{4}\left(Z^{n+1}_{i+1}+Z^{n}_{i}+Z^{n}_{i+1}+Z^{n+1}_{i}\right).\tag{16}$$

Substitution of the operator into multisymplectic Preissman scheme of Maxwell's equations, the complete scheme, can be shown in the following equations:

$$\begin{aligned}&\left(E^{n+1}_{x_{i,j+1,k+1}}+E^{n+1}_{x_{i,j,k+1}}+E^{n+1}_{x_{i,j+1,k}}+E^{n+1}_{x_{i,j,k}}\right)\\ &\quad-\frac{\Delta t}{\varepsilon\Delta y}\left(H^{n+1}_{z_{i,j+1,k+1}}+H^{n+1}_{z_{i,j+1,k}}-H^{n+1}_{z_{i,j,k+1}}-H^{n+1}_{z_{i,j,k}}\right)\\ &\quad+\frac{\Delta t}{\varepsilon\Delta z}\left(H^{n+1}_{y_{i,j+1,k+1}}+H^{n+1}_{y_{i,j,k+1}}-H^{n+1}_{y_{i,j+1,k}}-H^{n+1}_{y_{i,j,k}}\right)\\ &=\left(E^{n}_{x_{i,j+1,k+1}}+E^{n}_{x_{i,j,k+1}}+E^{n}_{x_{i,j+1,k}}+E^{n}_{x_{i,j,k}}\right)\\ &\quad+\frac{\Delta t}{\varepsilon\Delta y}\left(H^{n}_{z_{i,j+1,k+1}}+H^{n}_{z_{i,j+1,k}}-H^{n}_{z_{i,j,k+1}}-H^{n}_{z_{i,j,k}}\right)\\ &\quad-\frac{\Delta t}{\varepsilon\Delta z}\left(H^{n}_{y_{i,j+1,k+1}}+H^{n}_{y_{i,j,k+1}}-H^{n}_{y_{i,j+1,k}}-H^{n}_{y_{i,j,k}}\right)\end{aligned}\tag{17}$$

$$\begin{aligned}&\left(E^{n+1}_{y_{i+1,j,k+1}}+E^{n+1}_{y_{i,j,k+1}}+E^{n+1}_{y_{i+1,j,k}}+E^{n+1}_{y_{i,j,k}}\right)\\ &\quad-\frac{\Delta t}{\varepsilon\Delta z}\left(H^{n+1}_{x_{i+1,j,k+1}}+H^{n+1}_{x_{i,j,k+1}}-H^{n+1}_{x_{i+1,j,k}}-H^{n+1}_{x_{i,j,k}}\right)\\ &\quad+\frac{\Delta t}{\varepsilon\Delta x}\left(H^{n+1}_{z_{i+1,j,k+1}}+H^{n+1}_{z_{i+1,j,k}}-H^{n+1}_{z_{i,j,k+1}}-H^{n+1}_{z_{i,j,k}}\right)\\ &=\left(E^{n}_{y_{i+1,j,k+1}}+E^{n}_{y_{i,j,k+1}}+E^{n}_{y_{i+1,j,k}}+E^{n}_{y_{i,j,k}}\right)\\ &\quad+\frac{\Delta t}{\varepsilon\Delta z}\left(H^{n}_{x_{i+1,j,k+1}}+H^{n}_{x_{i,j,k+1}}-H^{n}_{x_{i+1,j,k}}-H^{n}_{x_{i,j,k}}\right)\\ &\quad-\frac{\Delta t}{\varepsilon\Delta x}\left(H^{n}_{z_{i+1,j,k+1}}+H^{n}_{z_{i+1,j,k}}-H^{n}_{z_{i,j,k+1}}-H^{n}_{z_{i,j,k}}\right)\end{aligned}\tag{18}$$

$$\begin{cases}\left(E^{n+1}_{z_{i+1,j+1,k}}+E^{n+1}_{z_{i,j+1,k}}+E^{n+1}_{z_{i+1,j,k}}+E^{n+1}_{z_{i,j,k}}\right)\\ \quad-\dfrac{\Delta t}{\varepsilon\Delta x}\left(H^{n+1}_{y_{i+1,j+1,k}}+H^{n+1}_{y_{i+1,j,k}}-H^{n+1}_{y_{i,j+1,k}}-H^{n+1}_{y_{i,j,k}}\right)\\ \quad+\dfrac{\Delta t}{\varepsilon\Delta y}\left(H^{n+1}_{x_{i+1,j+1,k}}+H^{n+1}_{x_{i,j+1,k}}-H^{n+1}_{x_{i+1,j,k}}-H^{n+1}_{x_{i,j,k}}\right)\\ =\left(E^{n}_{z_{i+1,j+1,k}}+E^{n}_{z_{i,j+1,k}}+E^{n}_{z_{i+1,j,k}}+E^{n}_{z_{i,j,k}}\right)\\ \quad+\dfrac{\Delta t}{\varepsilon\Delta x}\left(H^{n}_{y_{i+1,j+1,k}}+H^{n}_{y_{i+1,j,k}}-H^{n}_{y_{i,j+1,k}}-H^{n}_{y_{i,j,k}}\right)\\ \quad-\dfrac{\Delta t}{\varepsilon\Delta y}\left(H^{n}_{x_{i+1,j+1,k}}+H^{n}_{x_{i,j+1,k}}-H^{n}_{x_{i+1,j,k}}-H^{n}_{x_{i,j,k}}\right)\end{cases}\tag{20}$$

$$\begin{cases}\left(H^{n+1}_{x_{i,j+1,k+1}}+H^{n+1}_{x_{i,j,k+1}}+H^{n+1}_{x_{i,j+1,k}}+H^{n+1}_{x_{i,j,k}}\right)\\ \quad-\dfrac{\Delta t}{\mu\Delta z}\left(E^{n+1}_{y_{i,j+1,k+1}}+E^{n+1}_{y_{i,j,k+1}}-E^{n+1}_{y_{i,j+1,k}}-E^{n+1}_{y_{i,j,k}}\right)\\ \quad+\dfrac{\Delta t}{\mu\Delta y}\left(E^{n+1}_{z_{i,j+1,k+1}}+E^{n+1}_{z_{i,j+1,k}}-E^{n+1}_{z_{i,j,k+1}}-E^{n+1}_{z_{i,j,k}}\right)\\ =\left(H^{n}_{x_{i,j+1,k+1}}+H^{n}_{x_{i,j,k+1}}+H^{n}_{x_{i,j+1,k}}+H^{n}_{x_{i,j,k}}\right)\\ \quad+\dfrac{\Delta t}{\mu\Delta z}\left(E^{n}_{y_{i,j+1,k+1}}+E^{n}_{y_{i,j,k+1}}-E^{n}_{y_{i,j+1,k}}-E^{n}_{y_{i,j,k}}\right)\\ \quad-\dfrac{\Delta t}{\mu\Delta y}\left(E^{n}_{z_{i,j+1,k+1}}+E^{n}_{z_{i,j+1,k}}-E^{n}_{z_{i,j,k+1}}-E^{n}_{z_{i,j,k}}\right)\end{cases}\tag{21}$$

$$\begin{cases}\left(H^{n+1}_{y_{i+1,j,k+1}}+H^{n+1}_{y_{i,j,k+1}}+H^{n+1}_{y_{i+1,j,k}}+H^{n+1}_{y_{i,j,k}}\right)\\ \quad-\dfrac{\Delta t}{\mu\Delta x}\left(E^{n+1}_{z_{i+1,j,k+1}}+E^{n+1}_{z_{i+1,j,k}}-E^{n+1}_{z_{i,j,k+1}}-E^{n+1}_{z_{i,j,k}}\right)\\ \quad+\dfrac{\Delta t}{\mu\Delta z}\left(E^{n+1}_{x_{i+1,j,k+1}}+E^{n+1}_{x_{i,j,k+1}}-E^{n+1}_{x_{i+1,j,k}}-E^{n+1}_{x_{i,j,k}}\right)\\ =\left(H^{n}_{y_{i+1,j,k+1}}+H^{n}_{y_{i,j,k+1}}+H^{n}_{y_{i+1,j,k}}+H^{n}_{y_{i,j,k}}\right)\\ \quad+\dfrac{\Delta t}{\mu\Delta x}\left(E^{n}_{z_{i+1,j,k+1}}+E^{n}_{z_{i+1,j,k}}-E^{n}_{z_{i,j,k+1}}-E^{n}_{z_{i,j,k}}\right)\\ \quad-\dfrac{\Delta t}{\mu\Delta z}\left(E^{n}_{x_{i+1,j,k+1}}+E^{n}_{x_{i,j,k+1}}-E^{n}_{x_{i+1,j,k}}-E^{n}_{x_{i,j,k}}\right)\end{cases}\tag{22}$$

$$\begin{cases}\left(H^{n+1}_{z_{i+1,j+1,k}}+H^{n+1}_{z_{i,j+1,k}}+H^{n+1}_{z_{i+1,j,k}}+H^{n+1}_{z_{i,j,k}}\right)\\ \quad-\dfrac{\Delta t}{\mu\Delta y}\left(E^{n+1}_{z_{i+1,j+1,k}}+E^{n+1}_{z_{i,j+1,k}}-E^{n+1}_{z_{i+1,j,k}}-E^{n+1}_{z_{i,j,k}}\right)\\ \quad+\dfrac{\Delta t}{\mu\Delta x}\left(E^{n+1}_{y_{i+1,j+1,k}}+E^{n+1}_{y_{i+1,j,k}}-E^{n+1}_{y_{i,j+1,k}}-E^{n+1}_{y_{i,j,k}}\right)\\ =\left(H^{n}_{z_{i+1,j+1,k}}+H^{n}_{z_{i,j+1,k}}+H^{n}_{z_{i+1,j,k}}+H^{n}_{z_{i,j,k}}\right)\\ \quad+\dfrac{\Delta t}{\mu\Delta y}\left(E^{n}_{z_{i+1,j+1,k}}+E^{n}_{z_{i,j+1,k}}-E^{n}_{z_{i+1,j,k}}-E^{n}_{z_{i,j,k}}\right)\\ \quad-\dfrac{\Delta t}{\mu\Delta x}\left(E^{n}_{y_{i+1,j+1,k}}+E^{n}_{y_{i+1,j,k}}-E^{n}_{y_{i,j+1,k}}-E^{n}_{y_{i,j,k}}\right).\end{cases}\tag{23}$$

It can be observed that the aforementioned multisymplectic Preissman scheme is implicit, and the number of grid nodes is required to iterative E_z at the $n+1$ time step. To resolve the aforementioned system of equations, one may consider the multisymplectic Preissman scheme as a system of linear equations, arrange the pertinent variables, and utilize the coefficient matrix of the system of linear equations to solve them sequentially. However, the coefficient matrix in question is computationally extensive, requires a significant amount of memory, and is slow to solve. For instance, with 100 grids in each of the *x*-, *y*-, and z-directions, the matrix size balloons to 6 million $\times$6 million, leading to highly inefficient computations. This article proposes a simpler method to convert the 3-D Maxwell's equations into a form suitable for computation, reducing both computational memory requirements and enabling parallel processing.

Subsequently, the multisymplectic Hamiltonian equation was decomposed into a series of LOD MS-FDTD equations, demonstrating that the split LOD Hamiltonian equation continues to satisfy the MSCL and retains the characteristics of the original Hamiltonian equation, thereby confirming its viability. The equations can be presented as follows:

$$\frac{1}{m}\mathbf{M}Z_t+\mathbf{K_k}Z_x=\nabla z S_k(\mathbf{z}),\quad k=1,2,\ldots,m\tag{24}$$

where the function $S_k(\mathbf{z})$ can represent any splitting of $S(\mathbf{z})$, provided that it satisfies the MSCL criterion.

The multisymplectic Hamiltonian system can be decomposed into three subsystems of the LOD scheme, allowing for the LOD multisymplectic Preissman scheme for Maxwell's system to be expressed as follows:

$$\frac{1}{\Delta t/2}\left(E^{n+\frac12}_{y_{i+\frac12,j,k}}-E^{n}_{y_{i+\frac12,j,k}}\right)=-\frac{1}{\varepsilon}\delta_x\left(H^{n+\frac12}_{z_{i+\frac12,j,k}}+H^{n}_{z_{i+\frac12,j,k}}\right)\tag{25}$$

$$\frac{1}{\Delta t/2}\left(H^{n+\frac12}_{z_{i+\frac12,j,k}}-H^{n}_{z_{i+\frac12,j,k}}\right)=-\frac{1}{\mu}\delta_x\left(E^{n}_{y_{i,j,k}}+E^{n+\frac12}_{y_{i,j,k}}\right)\tag{26}$$

$$\frac{1}{\Delta t/2}\left(E^{n+\frac12}_{z_{i+\frac12,j,k}}-E^{n}_{z_{i+\frac12,j,k}}\right)=\frac{1}{\varepsilon}\delta_x\left(H^{n+\frac12}_{y_{i,j,k}}+H^{n}_{y_{i,j,k}}\right)\tag{27}$$

$$\frac{1}{\Delta t/2}\left(H^{n+\frac12}_{y_{i+\frac12,j,k}}-H^{n}_{y_{i+\frac12,j,k}}\right)=\frac{1}{\mu}\delta_x\left(E^{n}_{z_{i,j,k}}+E^{n+\frac12}_{z_{i,j,k}}\right)\tag{28}$$

$$\frac{1}{\Delta t/2}\left(E^{n+\frac12}_{x_{i,j+\frac12,k}}-E^{n}_{x_{i,j+\frac12,k}}\right)=\frac{1}{\varepsilon}\delta_y\left(H^{n+\frac12}_{z_{i,j,k}}+H^{n+1}_{z_{i,j,k}}\right)\tag{29}$$

$$\frac{1}{\Delta t/2}\left(H^{n+1}_{z_{i,j+\frac12,k}}-H^{n+\frac12}_{z_{i,j+\frac12,k}}\right)=\frac{1}{\mu}\delta_y\left(E^{n}_{x_{i,j,k}}+E^{n+\frac12}_{x_{i,j,k}}\right)\tag{30}$$

$$\frac{1}{\Delta t/2}\left(E^{n+1}_{z_{i,j+\frac12,k}}-E^{n+\frac12}_{z_{i,j+\frac12,k}}\right)=-\frac{1}{\varepsilon}\delta_y\left(H^{n+\frac12}_{x_{i,j,k}}+H^{n}_{x_{i,j,k}}\right)\tag{31}$$

$$\frac{1}{\Delta t/2}\left(H^{n+\frac12}_{x_{i,j+\frac12,k}}-H^{n}_{x_{i,j+\frac12,k}}\right)=-\frac{1}{\mu}\delta_y\left(E^{n+1}_{z_{i,j,k}}+E^{n+\frac12}_{z_{i,j,k}}\right)\tag{32}$$

$$\frac{1}{\Delta t/2}\left(E^{n+1}_{x_{i,j,k+\frac12}}-E^{n+\frac12}_{x_{i,j,k+\frac12}}\right)=-\frac{1}{\varepsilon}\delta_z\left(H^{n+1}_{y_{i,j,k}}+H^{n+\frac12}_{y_{i,j,k}}\right)\tag{33}$$

$$\frac{1}{\Delta t/2}\left(E^{n+1}_{y_{i,j,k+\frac12}}-E^{n+\frac12}_{y_{i,j,k+\frac12}}\right)=\frac{1}{\varepsilon}\delta_z\left(H^{n+1}_{x_{i,j,k}}+H^{n+\frac12}_{x_{i,j,k}}\right)\tag{34}$$

$$\frac{1}{\Delta t/2}\left(H^{n+1}_{x_{i,j,k+\frac12}}-H^{n+\frac12}_{x_{i,j,k+\frac12}}\right)=\frac{1}{\varepsilon}\delta_z\left(E^{n+1}_{y_{i,j,k}}+E^{n+\frac12}_{y_{i,j,k}}\right)\tag{35}$$

$$\frac{1}{\Delta t/2}\left(H^{n+1}_{y_{i,j,k+\frac12}}-H^{n+\frac12}_{y_{i,j,k+\frac12}}\right)=-\frac{1}{\varepsilon}\delta_z\left(E^{n+1}_{x_{i,j,k}}+E^{n+\frac12}_{x_{i,j,k}}\right).\tag{36}$$

Substituting the difference operator into the above equation gives the final Maxwell's equations in the LOD multisymplectic Preissman scheme

$$\begin{cases}\varepsilon_r(g_x)E^{n+\frac12}_{y_{i+1,j,k}}+\varepsilon_r(l)E^{n+\frac12}_{y_{i,j,k}}+\dfrac{\Delta t}{\varepsilon_0\Delta x}\left(H^{n+\frac12}_{z_{i+1,j,k}}-H^{n+\frac12}_{z_{i,j,k}}\right)\\ \quad=\varepsilon_r(g_x)E^{n}_{y_{i+1,j,k}}+\varepsilon_r(l)E^{n}_{y_{i,j,k}}-\dfrac{\Delta t}{\varepsilon\Delta x}\left(H^{n}_{z_{i+1,j,k}}-H^{n}_{z_{i,j,k}}\right)\\ \mu_r(g_x)H^{n+\frac12}_{z_{i+1,j,k}}+\mu_r(l)H^{n+\frac12}_{z_{i,j,k}}+\dfrac{\Delta t}{\mu_0\Delta x}\left(E^{n+\frac12}_{y_{i+1,j,k}}-E^{n+\frac12}_{y_{i,j,k}}\right)\\ \quad=\mu_r(g_x)H^{n}_{z_{i+1,j,k}}+\mu_r(l)H^{n}_{z_{i,j,k}}-\dfrac{\Delta t}{\mu_0\Delta x}\left(E^{n}_{y_{i+1,j,k}}-E^{n}_{y_{i,j,k}}\right)\end{cases}\tag{37}$$

$$\begin{cases} \varepsilon_r(g_x) E^{n+\frac{1}{2}}_{z_{i+1,j,k}} + \varepsilon_r(l) E^{n+\frac{1}{2}}_{z_{i,j,k}} - \dfrac{\Delta t}{\varepsilon \Delta x}\left(H^{n+\frac{1}{2}}_{y_{i+1,j,k}} - H^{n+\frac{1}{2}}_{y_{i,j,k}}\right) \\ \quad = \varepsilon_r(g_x) E^{n}_{z_{i+1,j,k}} + \varepsilon_r(l) E^{n}_{z_{i,j,k}} + \dfrac{\Delta t}{\varepsilon \Delta x}\left(H^{n}_{y_{i+1,j,k}} - H^{n}_{y_{i,j,k}}\right) \\ \mu_r(g_x) H^{n+\frac{1}{2}}_{y_{i+1,j,k}} + \mu_r(l) H^{n+\frac{1}{2}}_{y_{i,j,k}} - \dfrac{\Delta t}{\mu \Delta x}\left(E^{n+\frac{1}{2}}_{z_{i+1,j,k}} - E^{n+\frac{1}{2}}_{z_{i,j,k}}\right) \\ \quad = \varepsilon_r(g_x) H^{n}_{y_{i+1,j,k}} + \mu_r(l) H^{n}_{y_{i,j,k}} + \dfrac{\Delta t}{\mu \Delta x}\left(E^{n}_{z_{i+1,j,k}} - E^{n}_{z_{i,j,k}}\right) \end{cases} \tag{38}$$

$$\begin{cases} \varepsilon_r(g_y) E^{n+\frac{1}{2}}_{x_{i,j+1,k}} + \varepsilon_r(l) E^{n+\frac{1}{2}}_{x_{i,j,k}} - \dfrac{\Delta t}{\varepsilon \Delta y}\left(H^{n+1}_{z_{i,j+1,k}} - H^{n+1}_{z_{i,j,k}}\right) \\ \quad = \varepsilon_r(g_y) E^{n}_{x_{i,j+1,k}} + \varepsilon_r(l) E^{n}_{x_{i,j,k}} + \dfrac{\Delta t}{\varepsilon \Delta y}\left(H^{n+\frac{1}{2}}_{z_{i,j+1,k}} - H^{n+\frac{1}{2}}_{z_{i,j,k}}\right) \\ \mu_r(g_y) H^{n+1}_{z_{i,j+1,k}} + \mu_r(l) H^{n+1}_{z_{i,j,k}} - \dfrac{\Delta t}{\mu \Delta y}\left(E^{n+\frac{1}{2}}_{x_{i,j+1,k}} - E^{n+\frac{1}{2}}_{x_{i,j,k}}\right) \\ \quad = \mu_r(g_y) H^{n+\frac{1}{2}}_{z_{i,j+1,k}} + \mu_r(l) H^{n+\frac{1}{2}}_{z_{i,j,k}} + \dfrac{\Delta t}{\mu \Delta y}\left(E^{n}_{x_{i,j+1,k}} - E^{n}_{x_{i,j,k}}\right) \end{cases} \tag{39}$$

$$\begin{cases} \varepsilon_r(g_y) E^{n+1}_{z_{i,j+1,k}} + \varepsilon_r(l) E^{n+1}_{z_{i,j,k}} + \dfrac{\Delta t}{\varepsilon \Delta y}\left(H^{n+\frac{1}{2}}_{x_{i,j+1,k}} - H^{n+\frac{1}{2}}_{x_{i,j,k}}\right) \\ \quad = \varepsilon_r(g_y) E^{n+\frac{1}{2}}_{z_{i,j+1,k}} + \varepsilon_r(l) E^{n+\frac{1}{2}}_{z_{i,j,k}} - \dfrac{\Delta t}{\varepsilon \Delta y}\left(H^{n}_{x_{i,j+1,k}} - H^{n}_{x_{i,j,k}}\right) \\ \mu_r(g_y) H^{n+\frac{1}{2}}_{x_{i,j+1,k}} + \mu_r(l) H^{n+\frac{1}{2}}_{x_{i,j,k}} + \dfrac{\Delta t}{\mu \Delta y}\left(E^{n+1}_{z_{i,j+1,k}} - E^{n+1}_{z_{i,j,k}}\right) \\ \quad = \mu_r(g_y) H^{n}_{x_{i,j+1,k}} + \mu_r(l) H^{n}_{x_{i,j,k}} - \dfrac{\Delta t}{\mu \Delta y}\left(E^{n+\frac{1}{2}}_{z_{i,j+1,k}} - E^{n+\frac{1}{2}}_{z_{i,j,k}}\right) \end{cases} \tag{40}$$

$$\begin{cases} \varepsilon_r(g_z) E^{n+1}_{x_{i,j,k+1}} + \varepsilon_r(l) E^{n+1}_{x_{i,j,k}} + \dfrac{\Delta t}{\varepsilon \Delta z}\left(H^{n+1}_{y_{i,j,k+1}} - H^{n+1}_{y_{i,j,k}}\right) \\ \quad = \varepsilon_r(g_z) E^{n+\frac{1}{2}}_{x_{i,j,k+1}} + \varepsilon_r(l) E^{n+\frac{1}{2}}_{x_{i,j,k}} - \dfrac{\Delta t}{\varepsilon \Delta z}\left(H^{n+\frac{1}{2}}_{y_{i,j,k+1}} - H^{n+\frac{1}{2}}_{y_{i,j,k}}\right) \\ \mu_r(g_z) H^{n+1}_{y_{i,j,k+1}} + \mu_r(l) H^{n+1}_{y_{i,j,k}} + \dfrac{\Delta t}{\mu \Delta z}\left(E^{n+1}_{x_{i,j,k+1}} - E^{n+1}_{x_{i,j,k}}\right) \\ \quad = \mu_r(g_z) H^{n+\frac{1}{2}}_{y_{i,j,k+1}} + \mu_r(l) H^{n+\frac{1}{2}}_{y_{i,j,k}} - \dfrac{\Delta t}{\mu \Delta z}\left(E^{n+\frac{1}{2}}_{x_{i,j,k+1}} - E^{n+\frac{1}{2}}_{x_{i,j,k}}\right) \end{cases} \tag{41}$$

$$\begin{cases} \varepsilon_r(g_z) E^{n+1}_{y_{i,j,k+1}} + \varepsilon_r(l) E^{n+1}_{y_{i,j,k}} + \dfrac{\Delta t}{\varepsilon \Delta z}\left(H^{n+1}_{x_{i,j,k+1}} - H^{n+1}_{x_{i,j,k}}\right) \\ \quad = \varepsilon_r(g_z) E^{n+\frac{1}{2}}_{y_{i,j,k+1}} + \varepsilon_r(l) E^{n+\frac{1}{2}}_{y_{i,j,k}} - \dfrac{\Delta t}{\varepsilon \Delta z}\left(H^{n+\frac{1}{2}}_{x_{i,j,k+1}} - H^{n+\frac{1}{2}}_{x_{i,j,k}}\right) \\ \mu_r(g_z) H^{n+1}_{x_{i,j,k+1}} + \mu_r(l) H^{n+1}_{x_{i,j,k}} - \dfrac{\Delta t}{\mu \Delta z}\left(E^{n+1}_{y_{i,j,k+1}} - E^{n+1}_{y_{i,j,k}}\right) \\ \quad = \mu_r(g_z) H^{n+\frac{1}{2}}_{x_{i,j,k+1}} + \mu_r(l) H^{n+\frac{1}{2}}_{x_{i,j,k}} + \dfrac{\Delta t}{\mu \Delta z}\left(E^{n+\frac{1}{2}}_{y_{i,j,k+1}} - E^{n+\frac{1}{2}}_{y_{i,j,k}}\right) \end{cases} \tag{42}$$

with $g_x = (i+1, j, k), g_y = (i, j+1, k) g_z = (i, j, k+1), l = (i, j, k), m_x = (i-1, j, k), m_y = (i, j-1, k)$, and $m_z = (i, j, k-1)$.

Based on the aforementioned equation, it is apparent that the split MS-FDTD equations are straightforward to implement programmatically, leading to considerable reductions in computational workload and memory usage. However, due to the implicit nature of these equations, additional transformations are required. For instance, by substituting the electric field components from (37) into its magnetic field components, a tridiagonal matrix equation for the magnetic field components can be derived. This can then be solved in conjunction with the bidiagonal matrix equation for the electric field

$$\begin{cases} L_1 H^{n+\frac{1}{2}}_{z_{i,j-1,k}} + L_2 H^{n+\frac{1}{2}}_{z_{i,j,k}} + L_3 H^{n+\frac{1}{2}}_{z_{i,j+1,k}} \\ \quad = R_1 H^{n}_{z_{i,j-1,k}} + R_2 H^{n}_{z_{i,j,k}} + R_3 H^{n}_{z_{i,j+1,k}} \\ \qquad + R_4 E^{n}_{x_{i,j+1,k}} - R_5 E^{n}_{x_{i,j-1,k}} \end{cases} \tag{43}$$

$$\begin{cases} \varepsilon_r(g_y) E^{n+\frac{1}{2}}_{x_{i,j+1,k}} + \varepsilon_r(l) E^{n+\frac{1}{2}}_{x_{i,j,k}} + \dfrac{\Delta t}{\varepsilon_0 \Delta x}\left(H^{n+\frac{1}{2}}_{z_{i,j+1,k}} - H^{n+\frac{1}{2}}_{z_{i,j,k}}\right) \\ \quad = \varepsilon_r(g_y) E^{n}_{x_{i,j+1,k}} + \varepsilon_r(l) E^{n}_{x_{i,j,k}} - \dfrac{\Delta t}{\varepsilon_0 \Delta x}\left(H^{n}_{z_{i,j+1,k}} - H^{n}_{z_{i,j,k}}\right) \end{cases} \tag{44}$$

where

$$\begin{aligned} L_1 &= \varepsilon_r(m_y)\mu_r(m_y) - \frac{\Delta^2 t}{\varepsilon_0 \mu_0 \Delta^2 y} \\ L_2 &= 2\varepsilon_r(l)\mu_r(l) + \frac{2\Delta^2 t}{\varepsilon_0 \mu_0 \Delta^2 y} \\ L_3 &= \varepsilon_r(g_y)\mu_r(g_y) - \frac{\Delta^2 t}{\varepsilon_0 \mu_0 \Delta^2 y} \\ R_1 &= \varepsilon_r(m_y)\mu_r(m_y) + \frac{\Delta^2 t}{\varepsilon_0 \mu_0 \Delta^2 y} \\ R_2 &= 2\varepsilon_r(l)\mu_r(l) - \frac{2\Delta^2 t}{\varepsilon_0 \mu_0 \Delta^2 y} \\ R_3 &= \varepsilon_r(m_y)\mu_r(m_y) + \frac{\Delta^2 t}{\varepsilon_0 \mu_0 \Delta^2 y} \\ R_4 &= 2\varepsilon_r(g_y)\frac{\Delta t}{\mu_0 \Delta y} \\ R_5 &= 2\varepsilon_r(m_y)\frac{\Delta t}{\mu_0 \Delta y}, \quad R_6 = 2\mu_r(g_y)\frac{\Delta t}{\varepsilon_0 \Delta y} \\ R_7 &= 2\mu_r(m_y)\frac{\Delta t}{\varepsilon_0 \Delta y}. \end{aligned}$$

Furthermore, by substituting the magnetic field components into the electric field components, a tridiagonal matrix equation for the electric field components can be derived. This can then be solved in conjunction with the bidiagonal matrix equation for the magnetic field. The split MS-FDTD equations in two dimensions necessitate specific treatment, outlined by the following formulas:

$$\begin{cases} L_1 E^{n+\frac{1}{2}}_{z_{i-1,j}} + L_2 E^{n+\frac{1}{2}}_{z_{i,j}} + L_3 E^{n+\frac{1}{2}}_{z_{i+1,j}} \\ = R_1 E^{n}_{z_{i-1,j}} + R_2 E^{n}_{z_{i,j}} + R_3 E^{n}_{y_{i+1,j}} + R_6 H^{n}_{y_{i+1,j}} - R_7 H^{n}_{y_{i-1,j}} \end{cases} \tag{45}$$

$$\begin{cases} \mu_r(g_x) H^{n+1}_{y_{i+1,j}} + \mu_r(l) H^{n+1}_{y_{i,j}} - \dfrac{\Delta t}{\mu_0 \Delta x}\left(E^{n}_{z_{i+1,j}} - E^{n}_{z_{i,j}}\right) \\ = \mu_r(g_x) H^{n}_{y_{i+1,j}} + \mu_r(l) H^{n}_{y_{i,j}} + \dfrac{\Delta t}{\mu_0 \Delta x}\left(E^{n+\frac{1}{2}}_{z_{i+1,j}} - E^{n+\frac{1}{2}}_{z_{i,j}}\right) \end{cases} \tag{46}$$

$$\begin{cases} \left(L_1 E^{n+1}_{z_{i,j-1}} + L_2 E^{n+1}_{z_{i,j}} + L_3 E^{n+1}_{z_{i,j+1}}\right) \\ = R_1 E^{n+\frac{1}{2}}_{z_{i,j-1}} + R_2 E^{n+\frac{1}{2}}_{z_{i,j}} + R_3 E^{n+\frac{1}{2}}_{y_{i,j+1}} - R_4 H^{n}_{x_{i,j+1}} + R_5 H^{n}_{x_{i,j-1}} \end{cases} \tag{47}$$

$$\begin{cases} \varepsilon_r(g_y) H^{n+1}_{x_{i,j+1}} + \varepsilon_r(l) H^{n+1}_{x_{i,j}} + \dfrac{\Delta t}{\mu \Delta y}\left(E^{n+\frac{1}{2}}_{z_{i,j+1}} - E^{n+\frac{1}{2}}_{z_{i,j}}\right) \\ = \varepsilon_r(g_y) H^{n}_{x_{i,j+1}} + \mu_r(g_y) H^{n}_{x_{i,j}} - \dfrac{\Delta t}{\mu \Delta y}\left(E^{n+1}_{z_{i,j+1}} - E^{n+1}_{z_{i,j}}\right). \end{cases} \tag{48}$$

III. Numerical Stability and Dispersion Analysis

A. Numerical Stability Analysis

Section III utilize the Fourier method to analyze the stability of the algorithm proposed in this article. The matrix in the spatial spectral domain between the nth time step and the next $(n+1)$th time step is rewritten using the plane-wave solution of Maxwell's system of equations

$$\psi^{n+1} = \Lambda\psi^n = A^{-1}B\psi^n = C^{-1}D\psi^n. \tag{49}$$

The stability analysis of the MS-FDTD scheme is initially performed by matrixing all the coefficients in (7)–(12) and then substituting the plane-wave solution of Maxwell's system of equations into the matrix to obtain the matrices, as shown in the equation at the bottom of the page.

The eigenvalues of Λ are solved as

$$\lambda_1 = \lambda_2 = 1$$
$$\lambda_3 = \lambda_4 = -\frac{a-1+j\sqrt{4a}}{1+a}$$
$$\lambda_5 = \lambda_6 = -\frac{a-1-j\sqrt{4a}}{1+a}$$

where $a = (w_x^2+w_y^2+w_z^2)/(\varepsilon\mu)$, $w_x = c\sin(k_x\Delta x/2)\Delta t/\Delta x$, $w_y = c\sin(k_y\Delta y/2)\Delta t/\Delta y$, and $w_z = c\sin(k_z\Delta z/2)\Delta t/\Delta z$.

Therefore, we can conclude that the values of all eigenvalues are equal to 1, that is,

$$|\lambda| \equiv 1.$$

Therefore, the scheme of the MS-FDTD method is proved to be unconditionally stable. The unconditional stability of the MS-FDTD method can also be verified in the subsequent numerical examples.

In this article, the LOD of the MS-FDTD method is employed, necessitating additional stability analysis. Given that (37)–(42) are all locally 1-D schemes, we initially analyze the stability of the 1-D problems, utilizing the scheme outlined in (37) as a representative example. Initially, the coefficient matrix is derived in a manner similar to (7)–(12). Subsequently, by substituting the plane-wave solution of Maxwell's equations, the following coefficient matrix is obtained:

$$C = \begin{bmatrix} 1 & \frac{\Delta t}{2\varepsilon}\frac{\partial}{\partial x} \\ \frac{\Delta t}{2\mu}\frac{\partial}{\partial x} & 1 \end{bmatrix}, \quad D = \begin{bmatrix} 1 & -\frac{\Delta t}{2\varepsilon}\frac{\partial}{\partial x} \\ -\frac{\Delta t}{2\mu}\frac{\partial}{\partial x} & 1 \end{bmatrix}.$$

Upon solving for the eigenvalues, the following result is obtained:

$$\lambda_1 = -\frac{b-1+j\sqrt{4b}}{1+b}$$
$$\lambda_2 = -\frac{b-1-j\sqrt{4b}}{1+b}$$

where $b = w_x^2/(\varepsilon\mu)$ and $w_x = c\Delta t\sin(k_x\Delta x/2)/\Delta x$.

It can be demonstrated that for a given case, the modulus of the eigenvalues of matrix Λ is identically equal to 1, thereby proving the unconditional stability of (37). Similarly, the characteristic roots for (38)–(42) are identical. This indicates that all schemes from (37) to (42) exhibit unconditional stability at each substep, thereby confirming that the MS-FDTD method is both nondissipative and unconditionally stable.

$$A = \begin{bmatrix} 1 & 0 & 0 & 0 & \frac{\Delta t}{2\varepsilon}\frac{\partial}{\partial z} & -\frac{\Delta t}{2\varepsilon}\frac{\partial}{\partial y} \\ 0 & 1 & 0 & -\frac{\Delta t}{2\varepsilon}\frac{\partial}{\partial z} & 0 & \frac{\Delta t}{2\varepsilon}\frac{\partial}{\partial x} \\ 0 & 0 & 1 & \frac{\Delta t}{2\varepsilon}\frac{\partial}{\partial y} & -\frac{\Delta t}{2\varepsilon}\frac{\partial}{\partial x} & 0 \\ 0 & -\frac{\Delta t}{2\mu}\frac{\partial}{\partial z} & \frac{\Delta t}{2\mu}\frac{\partial}{\partial y} & 1 & 0 & 0 \\ \frac{\Delta t}{2\mu}\frac{\partial}{\partial z} & 0 & -\frac{\Delta t}{2\mu}\frac{\partial}{\partial x} & 0 & 1 & 0 \\ -\frac{\Delta t}{2\mu}\frac{\partial}{\partial x} & \frac{\Delta t}{2\mu}\frac{\partial}{\partial x} & 0 & 0 & 0 & 1 \end{bmatrix}$$

$$B = \begin{bmatrix} 1 & 0 & 0 & 0 & -\frac{\Delta t}{2\varepsilon}\frac{\partial}{\partial z} & \frac{\Delta t}{2\varepsilon}\frac{\partial}{\partial y} \\ 0 & 1 & 0 & \frac{\Delta t}{2\varepsilon}\frac{\partial}{\partial z} & 0 & -\frac{\Delta t}{2\varepsilon}\frac{\partial}{\partial x} \\ 0 & 0 & 1 & -\frac{\Delta t}{2\varepsilon}\frac{\partial}{\partial y} & \frac{\Delta t}{2\varepsilon}\frac{\partial}{\partial x} & 0 \\ 0 & \frac{\Delta t}{2\mu}\frac{\partial}{\partial z} & -\frac{\Delta t}{2\mu}\frac{\partial}{\partial y} & 1 & 0 & 0 \\ -\frac{\Delta t}{2\mu}\frac{\partial}{\partial z} & 0 & \frac{\Delta t}{2\mu}\frac{\partial}{\partial x} & 0 & 1 & 0 \\ \frac{\Delta t}{2\mu}\frac{\partial}{\partial x} & -\frac{\Delta t}{2\mu}\frac{\partial}{\partial x} & 0 & 0 & 0 & 1 \end{bmatrix}$$

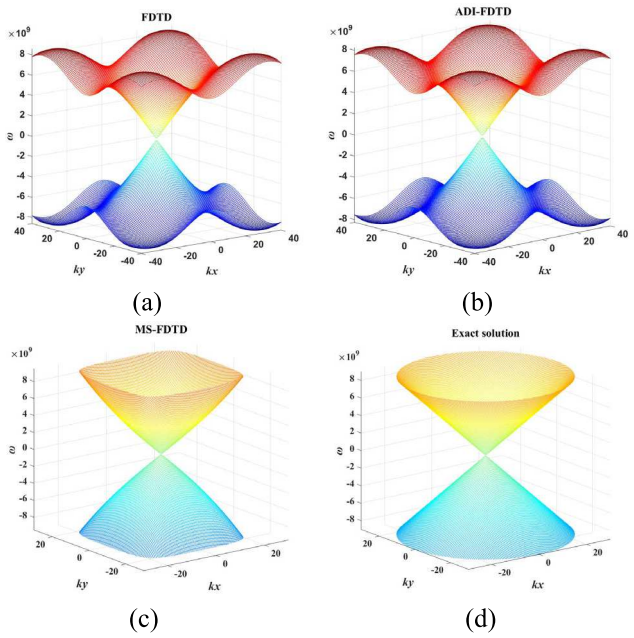

Fig. 1. Dispersion relations of the ADI-FDTD method, the FDTD method, and the MS-FDTD method at different frequencies. (a) FDTD method, (b) ADI-FDTD method, (c) MS-FDTD method, and (d) exact solution.

B. Numerical Dispersion Relation Analysis

The following equation represents the 3-D numerical dispersion relation of the MS-FDTD method:

$$\left(\frac{\tan\frac{\omega\Delta t}{2}}{c\Delta t}\right)^2=\left(\frac{\tan\left(\frac{k_x\Delta x}{2}\right)}{\Delta x}\right)^2+\left(\frac{\tan\left(\frac{k_y\Delta y}{2}\right)}{\Delta y}\right)^2+\left(\frac{\tan\left(\frac{k_z\Delta z}{2}\right)}{\Delta z}\right)^2. \tag{50}$$

In the following analysis, to examine the dispersion relations at different frequencies, Fig. 1 presents the dispersion relations for the MS-FDTD scheme, the FDTD method, and the ADI-FDTD method. It is important to note that the dispersion relation remains unchanged after applying the LOD splitting technique. This is because each substep in the splitting (LOD) MS-FDTD scheme preserves the same numerical dispersion characteristics as the original unsplit scheme, and the entire decomposition process does not alter the underlying dispersion relation. All three methods utilize identical uniform cells ($\Delta x = \Delta y = \Delta z = 0.1$ m) and adopt the same time step ($\Delta t = 1.667\text{e}^{-10}$ s).

As illustrated in Fig. 1, the dispersion relation of the MS-FDTD method is significantly better than that of the FDTD method. To visually highlight their distinctions, this study employs contour plots of dispersion relations using k_x and k_y as coordinates at a given frequency. Moreover, the contour figures projected onto the (k_x, k_z)-plane and (k_y, k_z)-plane are omitted, as they are identical to those of the (k_x, k_y)-plane due to the symmetric properties of the numerical dispersion relation. As illustrated in Fig. 2, the numerical contours are almost circular for small values of k, while the dispersion performance of both the FDTD and ADI-FDTD methods exhibits distortion in the edge regions and high-frequency areas, whereas the MS-FDTD method demonstrates superior dispersion performance. This improved dispersion accuracy can be partially attributed to the mathematical similarity between the MS-FDTD and higher order FDTD schemes, albeit at the expense of reduced computational efficiency.

IV. Numerical Results

In this section, we first present the new version of the grid distribution for the electric and magnetic field in Maxwell's equations based on the MS-FDTD scheme. Subsequently, several numerical examples are simulated and the results of the proposed MS-FDTD method are compared with the conventional FDTD method. An important condition used in numerical arithmetic is CFL number (i.e., CFLN = $\Delta t/\Delta t_{CFL}$), where Δt_{CFL} is the maximum stability limit of the FDTD method. The computer configuration is an Intel Core i7-13700K CPU (3.40 GHz) and 64-GB RAM (DDR4 3600 MHz).

A. Grid Point Distribution

The grid configurations of the MS-FDTD method differ significantly from those of the Yee schemes for the FDTD method. In the Yee scheme, the magnetic field components and electric field components are staggered, whereas the MS-FDTD scheme places magnetic and electric fields at the same grid point. For instance, considering $Ez_{i,j,k}$, $Ez_{i,j+1,k}$, $Ez_{i,j,k+1}$, and $Ez_{i,j+1,k+1}$ as a set of Ez components (similarly for Hx and Hy), the update of the Ez component at the $(n+1)$th time step requires the values of Hx and Hy from the $(n+1)$th time step, in addition to the values of Ez, Hx, and Hy from the nth time step. Figs. 3 and 4 depict the specific spatial distributions. In these figures, Hx and Hy at the $(n+1)$th time step are indicated in red, Ez and Ey at the $(n+1)$th time step are indicated in yellow, Hx and Hy at the nth time step are indicated in blue, and Ez and Ey at the nth time step are indicated in green.

B. Periodic Boundary Conditions

Based on the grid distribution outlined above, we developed PEC and periodic boundary conditions suitable for the MS-FDTD scheme. The PEC boundary is similar to that in traditional FDTD, so it will not be elaborated on here; instead, the focus will be on the periodic boundary. In the MS-FDTD scheme, decomposed by the LOD method, calculating a specific electric or magnetic field component requires only considering the component in one direction. To implement a periodic boundary in the x-direction, it is sufficient to handle the electric field components in (37) and (38) for this direction. For instance, in (38), $Ez_{1,j,k}$ and $Ez_{2,j,k}$ are treated as one group, while $Ez_{S,j,k}$ and $Ez_{S+1,j,k}$ are treated as another group. As shown in Fig. 5, by setting periodic boundaries at $x = 2$ and $x = \text{S}$, the following relationships can be obtained:

$$Ez(1,j,k)=Ez(S,j,k)$$
$$Ez(S+1,j,k)=Ez(2,j,k).$$

When solving the iterative formula with the electric field coefficient as a tridiagonal matrix and the magnetic field coefficient as a bidiagonal matrix, with periodic boundary

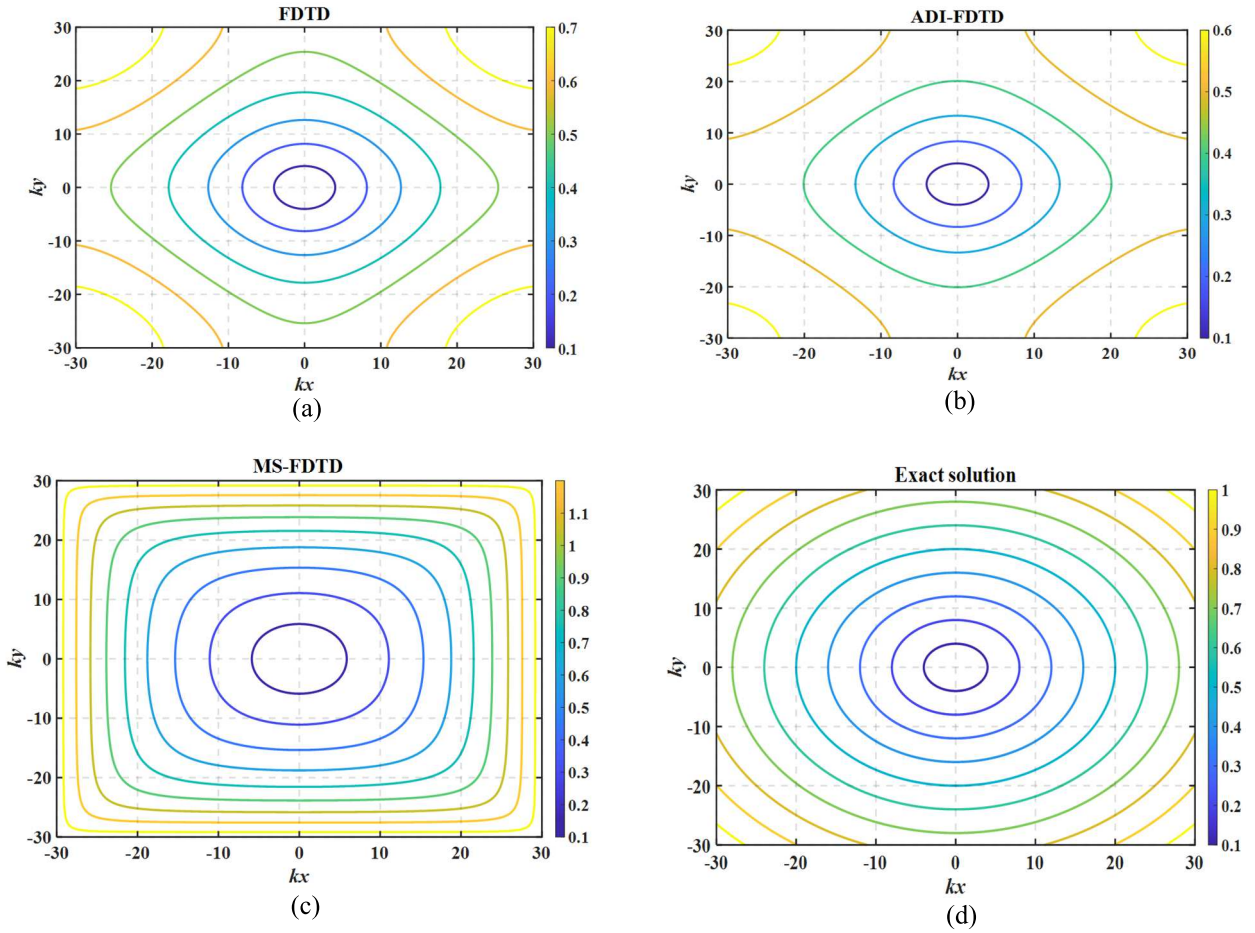

Fig. 2. Dispersion relations of the ADI-FDTD method, the FDTD method, and the MS-FDTD method at a specific frequency. (a) FDTD method, (b) ADI-FDTD method, (c) MS-FDTD method, and (d) exact solution.

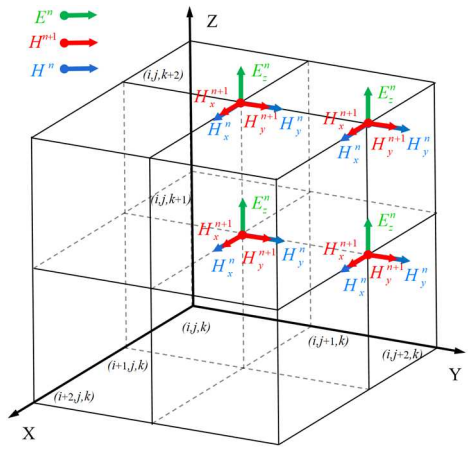

Fig. 3. Ez at time step $n+1$ with the illustrated related electric field components and magnetic field components.

conditions enforced between $x = 2$ and $x = \mathrm{S}$, the tridiagonal matrix requires the following special treatment:

$$\begin{bmatrix} b_1 & c_1 & & & & \\ a_2 & b_2 & c_2 & & & \\ & \bullet & \bullet & \bullet & & \\ & & \bullet & \bullet & \bullet & \\ & & & a_{s-1} & b_{s-1} & c_{s-1} \\ & & & & a_s & b_s \end{bmatrix}$$

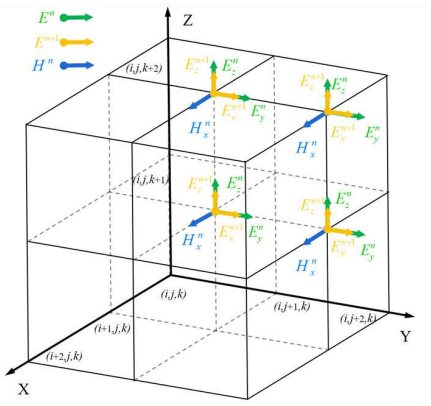

Fig. 4. Hx at time step $n+1$, with the illustrated related magnetic field components and electric field components.

$$\Rightarrow \begin{bmatrix} b_1 & c_1 & & & & \\ a_2 & b_2 & c_2 & & & a_2 \\ & \bullet & \bullet & \bullet & & \\ & & \bullet & \bullet & \bullet & \\ & & & a_{s-1} & b_{s-1} & c_{s-1} \\ & c_s & & & a_s & b_s \end{bmatrix}.$$

C. One-Dimensional Pulse Propagation

The same Gaussian pulse is defined by E(t) = E0∗exp[−[($t-t_0$)/τ]2] with $\tau = 1.0\mathrm{e}^{-8}$ s is used as the excitation source

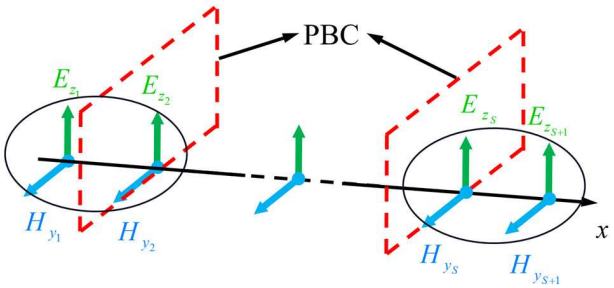

Fig. 5. Illustration of periodic boundary conditions at $x = 2$ and $x = S$ applied in the x-direction.

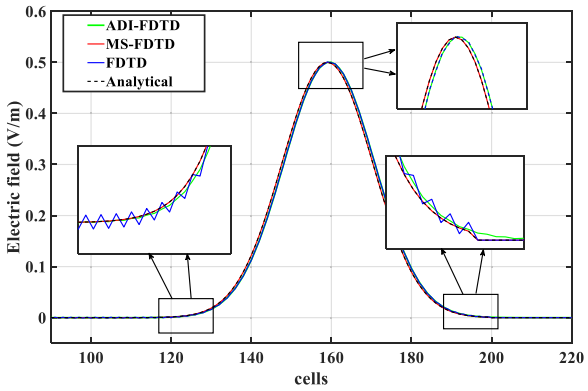

Fig. 6. Comparison of the time-domain waveforms for Gaussian pulse between the ADI-FDTD method, the MS-FDTD method, and the FDTD method.

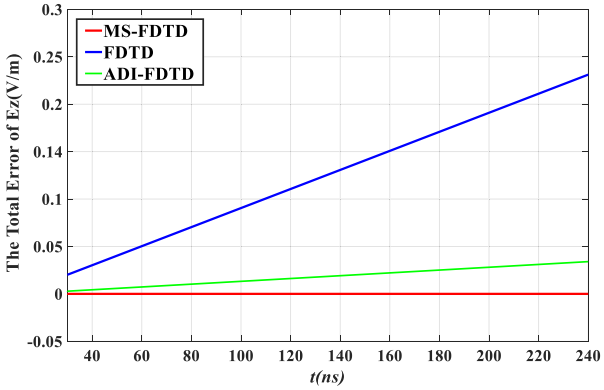

Fig. 7. Comparison of errors between the ADI-FDTD method, the FDTD method, and the MS-FDTD method with respect to the analytical solution.

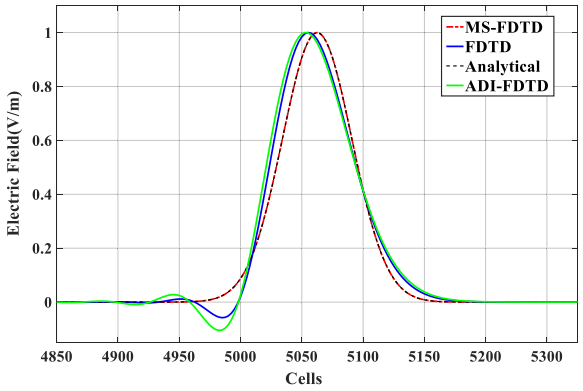

Fig. 8. Two-dimensional analysis of time-domain waveforms using the ADI-FDTD method, the MS-FDTD method, and the FDTD method with a Gaussian pulse; comparisons are made against the analytical solution waveform.

in simulations based on both the ADI-FDTD method, the MS-FDTD method, and the standard FDTD method. The spatial increment is set as 0.1 m, with a time step of $3.33e^{-10}$ s (CFLN = 1). When t_0 is defined to $2.5e^{-8}$ s, a minor, abrupt change in the waveform will be observed at the initial amplitude of the Gaussian pulse.

As illustrated in Fig. 6, after propagating for a certain distance, the waveform produced by the FDTD scheme exhibits significant jitter. This jitter includes small amplitude fluctuations throughout the entire waveform and distinct periodic oscillations between the two waveforms. The ADI-FDTD method shows noticeable improvement in reducing jitter compared to the FDTD method; however, it still suffers from evident waveform distortions. In contrast, the waveform of the MS-FDTD scheme is highly consistent with the waveform of the source, and the initial waveform of the Gaussian pulse source produces a mutation that remains consistent in the MS-FDTD scheme without additional mutation phenomena. Furthermore, the MS-FDTD scheme is a more suitable candidate in cases where a similarly specialized source is required.

For a more intuitive comparison of the differences between the two methods, as shown in Fig. 7, we generated graphs depicting the temporal evolution of errors between the MS-FDTD scheme and the analytical solution waveform, as well as between the FDTD scheme, the ADI-FDTD method, and the analytical solution waveform. It is evident that the error in the FDTD scheme increases over time, while the error in the ADI-FDTD method is significantly smaller. In contrast, the error in the MS-FDTD scheme remains nearly constant. This numerical example underscores that the MS-FDTD method effectively preserves the original waveform shape and maintains this fidelity over extended periods. It can be observed that, over extended iterations, the error in the FDTD method and the ADI-FDTD method progressively accumulates, whereas the MS-FDTD method maintains late-time stability.

D. Two-Dimensional Plane-Wave Propagation

For the 2-D numerical example, stability was first verified. The Gaussian source is the same as in the 1-D example, excited at the 50th cell and propagating along the x-direction, with the newly developed MS-FDTD scheme's periodic boundary conditions applied in the y-direction. According to the required magnetic and electric field components during iteration, the newly developed periodic boundary conditions involve multiple parameter adjustments for the tridiagonal matrix coefficients. The spatial increment is set as 0.1 m in all three directions. It is noteworthy that the MS-FDTD method employs a time step of $3.33e^{-10}$ s (CFL N = 1.41), whereas the FDTD method and the ADI-FDTD method use a time step of $2.12e^{-10}$ s (CFLN = 0.9). The waveforms generated by the three algorithms after propagating travels 5000 cells ($1e^{-6}$ s) are illustrated in Fig. 8. By utilizing different CFL conditions and maintaining the same actual physical time, the three algorithms effectively demonstrate the unconditional stability of the MS-FDTD method. The waveform produced by the FDTD method and the ADI-FDTD method exhibits significant

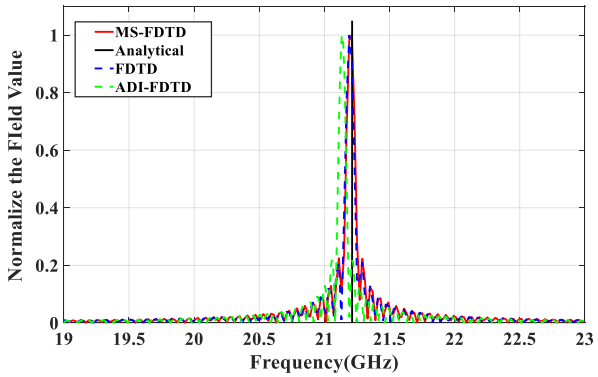

Fig. 9. Comparison of numerical and analytical results for single cavity mode in the ADI-FDTD method, the FDTD method, and the MS-FDTD method.

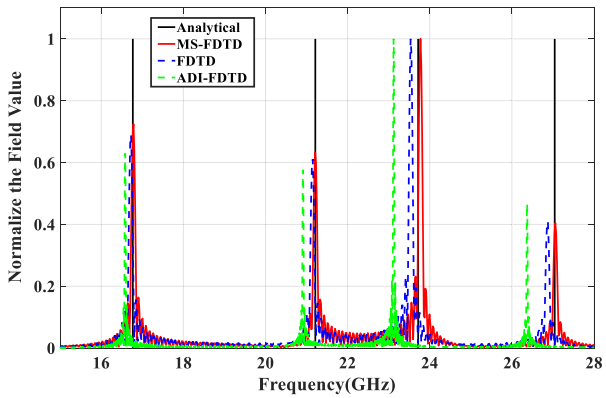

Fig. 10. Comparison of numerical and analytical results for multiple cavity modes in the ADI-FDTD method, the MS-FDTD method, and the FDTD method.

trailing, while the waveform generated by the MS-FDTD method closely matches the analytical solution as illustrated in Fig. 8. The MS-FDTD method and the ADI-FDTD method have been observed to exhibit greater stability than the FDTD method.

E. Cavity Modes

Furthermore, to analyze the accuracy of the MS-FDTD method, the resonant modes of a cavity were simulated. Due to the significant differences in the magnetic and electric field distributions between the MS-FDTD method and the FDTD method, the PEC boundary required for cavity modes needs to be redeveloped. Initially, a 0.01×0.01 m 2-D waveguide resonant cavity underwent single-mode testing with a spatial increment of $5e^{-4}$ m. To enhance the accuracy of the FDTD method, a time step of $1.67e^{-12}$ s (CFLN = 0.7) is adopted. In comparison, due to the unconditional stability of the MS-FDTD method, a time step of $3.3e^{-12}$ s (CFLN = 1.41) is employed. After the same amount of real physical time has elapsed. Fig. 9 illustrates that the resonant mode of the cavity, as simulated by the MS-FDTD method, is 21.2112 GHz. This result is closer to the analytical solution (21.2132 GHz) compared to the FDTD method, which produced a result of 21.1912 GHz. Moreover, the ADI-FDTD method performs the worst among the three, producing the least accurate result. The numerical efficiency of the three methods is nearly comparable.

To better discern the differences between the two algorithms, we increased the cavity size to 0.02×0.02 m while keeping the CFL condition unchanged, for multimode analysis (TE_{12}, TE_{22}, TE_{23}, and TE_{33}). As depicted in Fig. 10, numerical results for all four modes in the MS-FDTD scheme surpassed those of the FDTD method. The ADI-FDTD method produced less accurate results compared to the other two methods and is thus mainly excluded from direct comparison here. Specifically, the FDTD method exhibited a numerical error of 0.46%, in the TE_{33} mode, whereas the MS-FDTD scheme showed only 0.005% error. Detailed numerical results for the four cavity modes are presented in Table I, demonstrating that the MS-FDTD scheme provided results closer to the analytical solution with errors below 0.02%, highlighting its high precision. The FDTD method performed worse than the MS-FDTD scheme, while the ADI-FDTD method delivered the least accurate results. As illustrated in Fig. 10 and detailed in Table I, under relaxed CFL conditions, the MS-FDTD method not only achieves higher accuracy but also

TABLE I
NUMERICAL RESULTS OF THE CAVITY MODE

	FDTD		ADI-FDTD		Analytical
Modes	Frequency (GHz)	Error	Frequency (GHz)	Error	Frequency (GHz)
TE_{12}	16.7267	0.26%	16.5843	1.11%	16.7705
TE_{22}	21.1712	0.20%	20.9142	1.41%	21.2132
TE_{23}	23.5735	0.61%	23.1196	2.52%	23.7171
TE_{33}	26.9169	0.46%	26.3693	2.49%	27.0416
Time	1.4908s		1.9477s		
	MS-FDTD(Proposed)				Analytical
Modes	Frequency (GHz)	Error			Frequency (GHz)
TE_{12}	16.7668	0.02%			16.7705
TE_{22}	21.2112	0.001%			21.2132
TE_{23}	23.7738	0.02%			23.7171
TE_{33}	27.0554	0.005%			27.0416
Time	0.9092s				

demonstrates greater computational efficiency. Under identical computational settings and real-time simulation conditions, the MS-FDTD scheme achieved a runtime of 0.9092 s, compared to 1.4908 s for the FDTD method and 1.9477 s for the ADI-FDTD method. Multimodal computations revealed a distinct advantage of the MS-FDTD scheme over the FDTD method.

Furthermore, due to the unconditional stability, a more relaxed CFL condition can be chosen; the MS-FDTD scheme demonstrated significant computational time savings. Additionally, Table II presents the numerical results and computation times for cavity modes under different CFL settings in the MS-FDTD scheme, confirming its unconditional stability. Fig. 11 offers a more intuitive insight into the numerical results of cavity modes under varying CFL conditions. With increasing CFL values, the computed results for all four modes decrease and diverge from the analytical solution. When the CFLN is set to 1.27, the numerical results obtained using the MS-FDTD method are most closely aligned with the analytical solution.

F. Human Skin Model

To further validate the performance of the MS-FDTD scheme, its numerical accuracy was investigated through simulations using human skin as a medium. It is well established that the human body is a dispersive medium, exhibiting

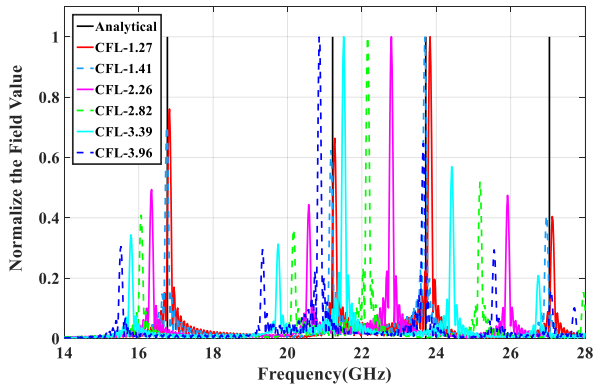

Fig. 11. Numerical calculation results of cavity modes in the MS-FDTD scheme under different CFL conditions.

TABLE II
NUMERICAL RESULTS OF THE MS-FDTD METHOD UNDER DIFFERENT CFL CONDITIONS

Modes	TE_{12}	TE_{22}	TE_{23}	TE_{33}
CFLN		Frequency (GHz)		
1.27	16.7814	21.2112	23.7738	27.0554
1.41	16.7668	21.1712	23.6937	26.957
2.26	16.3463	20.5706	22.7928	25.9159
2.82	16.0661	20.1702	22.1522	25.1752
3.39	15.7858	19.7497	21.5115	24.4144
3.96	15.5255	19.3293	20.8509	23.6537

CFLN	*The number of iterations*	*Time(s)*
1.27	12222	0.9617
1.41	11000	0.9092
2.26	6875	0.5127
2.82	5500	0.4438
3.39	4583	0.3855
3.96	3929	0.3474

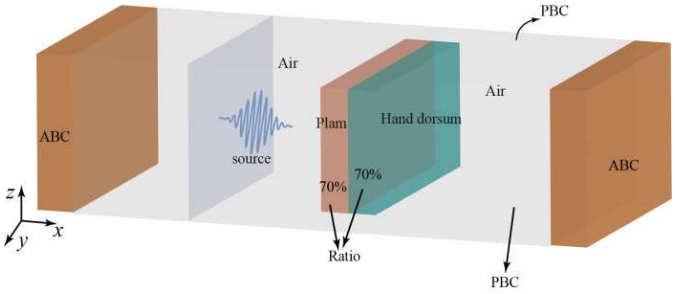

Fig. 12. Computational model of human skin medium includes a Gaussian source propagating along the x-direction, with periodic boundaries in the y- and z-directions. The model also includes two types of media, representing the palm and the hand dorsum.

dielectric constant variations with frequency. The issue of dispersive medium for the MS-FDTD scheme has not been addressed in this article, which will be the subject of further articles. For the purposes of this article, it is simplified here. The dielectric constant of skin remains relatively stable within a certain frequency range, enabling it to be approximated as a constant. Within this frequency range, the dielectric constant of the palm is set to 25 and that of the hand dorsum is set to 35. As shown in Fig. 12, the 3-D computational domain is configured with dimensions of $130 \times 20 \times 20$ cells. In the y-direction, the proportions of the two media to air are both

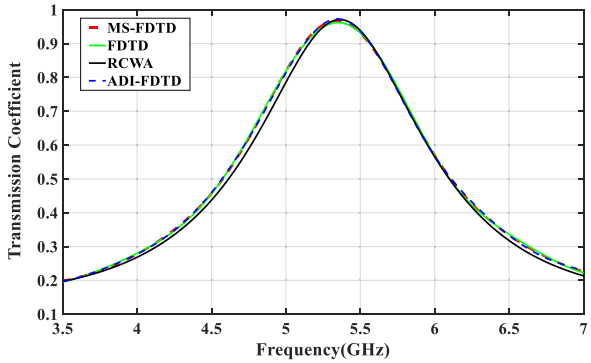

Fig. 13. Comparison of numerical and analytical results for transmission coefficient calculation in the ADI-FDTD method, the FDTD method, and the MS-FDTD method.

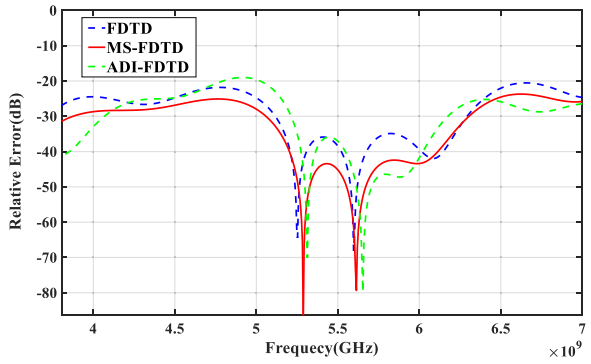

Fig. 14. Relative error comparison between the ADI-FDTD method, the MS-FDTD method and RCWA, and the FDTD method and RCWA.

set at 7:3, and spatial increments are uniformly set to $6e^{-5}$ m. The time increment for the MS-FDTD method is set to $1.15e^{-12}$ s (CFLN = 10), while for the FDTD method and the ADI-FDTD method, it is set to $1.15e^{-13}$ s (CFLN = 1). A Gaussian source propagates in the x-direction, while the periodic boundary conditions of the MS-FDTD scheme are applied in the other two directions. Depending on the required magnetic and electric field components during the iteration, the periodic boundary conditions necessitate multiple parameter adjustments to the tridiagonal matrix coefficients.

The dimensions of the palm and the hand dorsum are both set to $3e^{-3}$ m, and the specific modeling diagram is shown in Fig. 12. As shown in Fig. 13, the numerical results of all three methods closely agree with those of the rigorous coupled wave analysis (RCWA), with the MS-FDTD method exhibiting a slight advantage across the entire frequency band. To elucidate the differences between the MS-FDTD method, the ADI-FDTD method, and the FDTD method more clearly, we have generated a relative error graph, as presented in Fig. 14. The relative error is defined as: $20log10(|T_1 - T_0|/T_0)$, where T_1 represents the transmission coefficient results calculated by the MS-FDTD method, the ADI-FDTD method, and the FDTD method, and T_0 represents the transmission coefficient results calculated by RCWA. It is evident that across the calculated frequency range, the accuracy of the MS-FDTD method is consistently higher than that of the ADI-FDTD method. Compared to the FDTD method, the MS-FDTD method yields results that are very similar; however, from an overall perspective, the MS-FDTD method demonstrates a clear advantage. The

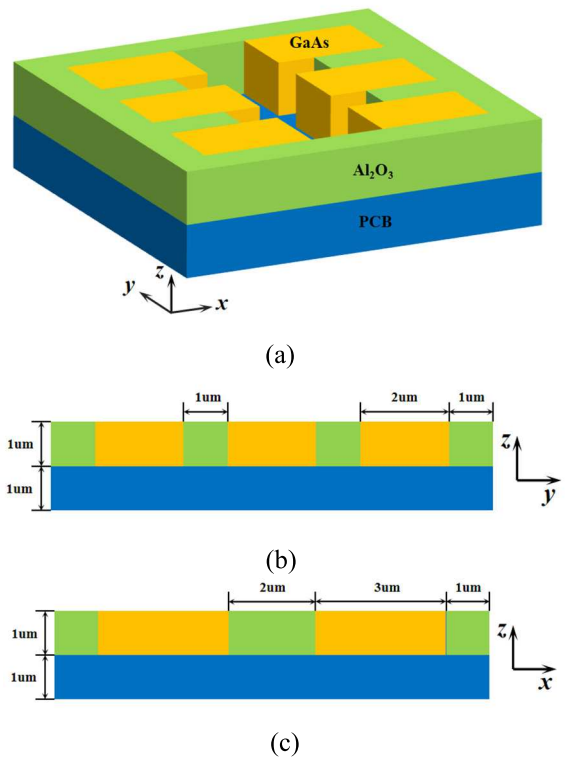

Fig. 15. Geometric shape of the onboard chip. (a) Overview. (b) *yz* cross section. (c) *xz* cross section.

MS-FDTD method adopts a more relaxed CFL condition, which, although it introduces a relatively higher computational workload per iteration, completes the simulation in 63.12 s. This is significantly faster than the conventional FDTD method (94.41 s) and much faster than the ADI-FDTD method, which requires 520.32 s.

G. Onboard Chip

In the final analysis, an electric field amplitude evaluation was performed on the onboard chip model to assess the MS-FDTD method's capability in accurately handling complex structures. The chip model configuration and dimensions are illustrated in Fig. 15, where the dielectric constants for GaAs and Al_2O_3 are set to 12 and 8, respectively. A Gaussian source, consistent with those used in earlier simulations, was employed, with the point source placed at the center of the model to ensure uniform propagation, while all external boundaries were defined using PEC boundary conditions to confine the field within the model. The simulation was conducted on $50 \times 50 \times 50$ cells, a size chosen to balance accuracy and computational efficiency, with both the MS-FDTD and conventional FDTD methods, and ADI-FDTD methods all using a spatial step size of $2.5e^{-7}$ m to maintain comparable resolution across the grid. For temporal accuracy, the MS-FDTD method used a time step size of $9.68e^{-16}$ s (CFLN = 2), while the time step size for both the FDTD method and the ADI-FDTD method was set to $4.84e^{-1}6$ s (CFLN = 1), thereby ensuring stability and enabling a direct performance comparison under controlled conditions. Additionally, commercial software COMSOL was used for the verification of both methods.

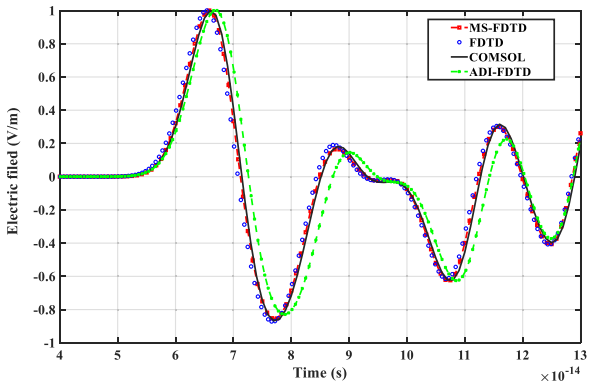

Fig. 16. Electric field amplitude after passing through the onboard chip.

TABLE III
SIMULATION STEPS AND SIMULATION TIME

	FDTD	ADI-FDTD	MS-FDTD	COMSOL
Time Step (s)	4.84×10^{-16}	9.68×10^{-16}	9.68×10^{-16}	2.8×10^{-15}
Number of Iterations	40000	20000	20000	6915
Simulation Time (s)	461.65	370.84	382.31	1.26×10^{5}
memory	16.7MB	34.6MB	35.4MB	76GB

As shown in Fig. 16, after the same amount of real physical time ($1.92e^{-11}$ s), the electric field amplitudes measured at the same spatial location across the simulation domain for both methods, along with the COMSOL simulation results, show excellent agreement. The ADI-FDTD method, however, exhibits relatively poor accuracy. Notably, the MS-FDTD method results demonstrate higher accuracy compared to the FDTD method when benchmarked against COMSOL. This highlights the accuracy and stability of the MS-FDTD method in simulating electric field behavior within complex materials. As shown in Table III, under the more relaxed CFL conditions, the MS-FDTD method demonstrates superior efficiency, with a computation time of 382.31 s, significantly lower than the FDTD method's 461.65 s and COMSOL's computation time. However, the computation time of the MS-FDTD method is slightly longer than that of the ADI-FDTD method (370.84 s). This is because, compared to the ADI-FDTD method, the MS-FDTD method needs to handle additional bidiagonal matrices. For the same reason, the MS-FDTD method requires slightly more memory than the ADI-FDTD method. Nevertheless, it remains significantly more memory-efficient than COMSOL, which demands substantial memory resources for mesh-based matrix assembly and storage, with matrix sizes potentially reaching up to 76 GB for large-scale simulations. While the MS-FDTD method requires somewhat more memory than the standard FDTD method, it still offers a manageable memory footprint, typically in the range of a few megabytes. This makes it a practical choice for large-scale simulations that require both high accuracy and efficient memory usage.

V. CONCLUSION

This article integrates the multisymplectic algorithm with computational electromagnetics for the first time and validates

its advantages in solving Maxwell's equations. Through a local 1-D approach, we have significantly reduced the computational burden of the multisymplectic Preissman scheme, though its efficiency remains slightly inferior to conventional FDTD methods. Additionally, the computational effort of the multisymplectic Preissman scheme is reduced by a local 1-D approach. Furthermore, for the first time, the distribution of grid for the multisymplectic Preissman scheme is provided in order to realize the time and space iterations based on the FDTD method to simulate electromagnetic problems. In addition, the stability of the multisymplectic algorithm is demonstrated by verifying that both the multisymplectic Preissman scheme and the MS-FDTD scheme are unconditionally stable. Finally, the advantages of the multisymplectic Preissman algorithm are demonstrated through a series of numerical examples, ranging from 1-D to 3-D scenarios. The algorithm is shown to have significant advantages, including late-time stability, high accuracy, and unconditional stability. In conclusion, the multisymplectic Preissman algorithm is applicable in the field of electromagnetic society, which represents a novel promising research direction in numerical computation.

REFERENCES

[1] Y. Wang, Y. Cheng, X.-H. Wang, S. Yang, and Z. Chen, "An SBP-SAT FDTD subgridding method using staggered Yee's grids without modifying field components for TM analysis," *IEEE Trans. Microw. Theory Techn.*, vol. 71, no. 2, pp. 579–592, Feb. 2023.

[2] L. Deng et al., "A symmetric FDTD subgridding method with guaranteed stability and arbitrary grid ratio," *IEEE Trans. Antennas Propag.*, vol. 71, no. 12, pp. 9207–9221, Dec. 2023.

[3] Y. Wang, Z. Chen, J. Wang, and P. Wang, "Three-dimensional simple conformal symplectic particle-in-cell method for simulations of high power microwave devices," in *Proc. IEEE Int. Vac. Electron. Conf. (IVEC)*, Apr. 2015, pp. 1–2.

[4] F. Zheng, Z. Chen, and J. Zhang, "A finite-difference time-domain method without the courant stability conditions," *IEEE Microw. Guided Wave Lett.*, vol. 9, no. 11, pp. 441–443, Nov. 1999.

[5] J.-B. Wang, B.-H. Zhou, L. Shi, and B. Chen, "Unconditionally stable FDTD method based on LOD scheme for analysis of 2-D periodic structures," *IEEE Trans. Antennas Propag.*, vol. 60, no. 8, pp. 4003–4006, Aug. 2012.

[6] E. L. Tan, "Unconditionally stable LOD–FDTD method for 3-D Maxwell's equations," *IEEE Microw. Wireless Compon. Lett.*, vol. 17, no. 2, pp. 85–87, Feb. 2007.

[7] D. Y. Heh and E. L. Tan, "Multiple LOD-FDTD method for inhomogeneous coupled transmission lines and stability analyses," *IEEE Trans. Antennas Propag.*, vol. 68, no. 3, pp. 2198–2205, Mar. 2020.

[8] J. Shibayama, M. Muraki, J. Yamauchi, and H. Nakano, "Efficient implicit FDTD algorithm based on locally one-dimensional scheme," *Electron. Lett.*, vol. 41, no. 19, pp. 1046–1047, Sep. 2005.

[9] S.-C. Yang, Z. Chen, Y. Yu, and W.-Y. Yin, "An unconditionally stable one-step arbitrary-order leapfrog ADI-FDTD method and its numerical properties," *IEEE Trans. Antennas Propag.*, vol. 60, no. 4, pp. 1995–2003, Apr. 2012.

[10] T. Namiki, "A new FDTD algorithm based on alternating-direction implicit method," *IEEE Trans. Microw. Theory Techn.*, vol. 47, no. 10, pp. 2003–2007, Oct. 1999.

[11] K. Niu et al., "Ultra-low frequency electromagnetic wave analysis in ocean-ionosphere based on ADI-FDTD combined with SIBC," *IEEE Trans. Antennas Propag.*, early access, Sep. 18, 2025, doi: 10.1109/TAP.2025.3608798.

[12] J. Chen, J. Li, and Q. H. Liu, "Designing graphene-based absorber by using HIE-FDTD method," *IEEE Trans. Antennas Propag.*, vol. 65, no. 4, pp. 1896–1902, Apr. 2017.

[13] J. Wang, B. Zhou, L. Shi, C. Gao, and B. Chen, "A novel 3-D HIE-FDTD method with one-step leapfrog scheme," *IEEE Trans. Microw. Theory Techn.*, vol. 62, no. 6, pp. 1275–1283, Jun. 2014.

[14] P. Wu, J. Wang, H. Jiang, Y. Xie, and T. Natsuki, "Fundamental weaker HIE-PML algorithm with simple implementation and enlarged time step for fine details along a single direction," *IEEE Trans. Microw. Theory Techn.*, vol. 72, no. 1, pp. 74–90, Jan. 2024.

[15] P. Wu, Y. Zhang, H. Jiang, Y. Xie, and T. Natsuki, "Fundamental higher order weaker HIE-PML algorithm for magnetized plasma," *IEEE Antennas Wireless Propag. Lett.*, vol. 23, pp. 2481–2485, 2024.

[16] K. Niu et al., "Transient electromagnetic–thermal co-simulation of microwave/RF integrated circuits by the HIE-FDTD method," *IEEE Trans. Microw. Theory Techn.*, vol. 72, no. 9, pp. 5228–5244, Sep. 2024.

[17] J. Chen, J. Li, and Q. H. Liu, "Analyzing graphene-based absorber by using the WCS-FDTD method," *IEEE Trans. Microw. Theory Techn.*, vol. 65, no. 10, pp. 3689–3696, Oct. 2017.

[18] J. Chen and J. Wang, "A novel WCS-FDTD method with weakly conditional stability," *IEEE Trans. Electromagn. Compat.*, vol. 49, no. 2, pp. 419–426, May 2007.

[19] J. Wang and W.-Y. Yin, "Development of a novel FDTD (2, 4)-compatible conformal scheme for electromagnetic computations of complex curved PEC objects," *IEEE Trans. Antennas Propag.*, vol. 61, no. 1, pp. 299–309, Jan. 2013.

[20] K. Niu et al., "A stochastic FDTD algorithm for uncertainty quantification of electromagnetic-thermal simulation," *IEEE Trans. Microw. Theory Techn.*, vol. 72, no. 7, pp. 3935–3946, Jul. 2024.

[21] K. Niu, Z. Huang, X. Ren, M. Li, B. Wu, and X. Wu, "An optimized 3-D HIE-FDTD method with reduced numerical dispersion," *IEEE Trans. Antennas Propag.*, vol. 66, no. 11, pp. 6435–6440, Nov. 2018.

[22] K. Niu, Z. Huang, M. Li, and X. Wu, "Optimization of the artificially anisotropic parameters in WCS-FDTD method for reducing numerical dispersion," *IEEE Trans. Antennas Propag.*, vol. 65, no. 12, pp. 7389–7394, Dec. 2017.

[23] K. Feng, "On difference schemes and symplectic geometry," in *Proc. Beijing Symp. Differ. Geometry Differ. Equ., Comput. Partial Differ. Equ.*, 1985, pp. 42–58.

[24] R. D. Ruth, "A canonical integration technique," *IEEE Trans. Nucl. Sci.*, vol. 30, no. 4, pp. 2669–2671, Mar. 1983.

[25] W. Sha, Z. Huang, M. Chen, and X. Wu, "Survey on symplectic finite-difference time-domain schemes for Maxwell's equations," *IEEE Trans. Antennas Propag.*, vol. 56, no. 2, pp. 493–500, Feb. 2008.

[26] W. Sha, Z. Huang, X. Wu, and M. Chen, "Application of the symplectic finite-difference time-domain scheme to electromagnetic simulation," *J. Comput. Phys.*, vol. 225, no. 1, pp. 33–50, Jul. 2007.

[27] W. Sha, X. Wu, M. Chen, and Z. Huang, "Application of the high-order symplectic FDTD scheme to the curved three-dimensional perfectly conducting objects," *Microw. Opt. Technol. Lett.*, vol. 49, no. 4, pp. 931–934, Apr. 2007.

[28] X. Ren et al., "High-order unified symplectic FDTD scheme for the metamaterials," *Comput. Phys. Commun.*, vol. 183, no. 6, pp. 1192–1200, Jun. 2012.

[29] T. Hirono, W. Lui, S. Seki, and Y. Yoshikuni, "A three-dimensional fourth-order finite-difference time-domain scheme using a symplectic integrator propagator," *IEEE Trans. Microw. Theory Techn.*, vol. 49, no. 9, pp. 1640–1648, Sep. 2001.

[30] T. J. Bridges and S. Reich, "Multi-symplectic integrators: Numerical schemes for Hamiltonian PDEs that conserve symplecticity," *Phys. Lett. A*, vol. 284, nos. 4–5, pp. 184–193, Jun. 2001.

[31] J. E. Marsden, G. W. Patrick, and S. Shkoller, "Multisymplectic geometry, variational integrators, and nonlinear PDEs," *Commun. Math. Phys.*, vol. 199, no. 2, pp. 351–395, Dec. 1998.

[32] P. E. Hydon, "Multisymplectic conservation laws for differential and differential-difference equations," *Proc. Roy. Soc. A, Math., Phys. Eng. Sci.*, vol. 461, no. 2058, pp. 1627–1637, Jun. 2005.

[33] Y. Sun and P. S. P. Tse, "Symplectic and multisymplectic numerical methods for Maxwell's equations," *J. Comput. Phys.*, vol. 230, no. 5, pp. 2076–2094, Mar. 2011.

[34] W. Yu-Shun, W. Bin, and C. Xin, "Multisymplectic Euler box scheme for the KdV equation," *Chin. Phys. Lett.*, vol. 24, no. 2, pp. 312–314, Feb. 2007.

[35] T. Liu and M. Qin, "Multisymplectic geometry and multisymplectic preissman scheme for the KP equation," *J. Math. Phys.*, vol. 43, no. 8, pp. 4060–4077, Aug. 2002.

[36] J.-B. Chen, "Multisymplectic geometry, local conservation laws and a multisymplectic integrator for the Zakharov–Kuznetsov equation," *Lett. Math. Phys.*, vol. 63, no. 2, pp. 115–124, Feb. 2003.

[37] J. Chen, "New schemes for the nonlinear Schrödinger equation," *Appl. Math. Comput.*, vol. 124, no. 3, pp. 371–379, Dec. 2001.

[38] J. Cai, Y. Wang, B. Wang, and B. Jiang, "New multisymplectic self-adjoint scheme and its composition scheme for the time-domain Maxwell's equations," *J. Math. Phys.*, vol. 47, no. 12, p. 18, Dec. 2006.
[39] H. J. Zhu, S. H. Song, and Y. M. Chen, "Multi-symplectic wavelet collocation method for Maxwell's equations," *Adv. Appl. Math. Mech.*, vol. 3, no. 6, pp. 663–688, Dec. 2011.
[40] L. Kong, J. Hong, and J. Zhang, "Splitting multisymplectic integrators for Maxwell's equations," *J. Comput. Phys.*, vol. 229, no. 11, pp. 4259–4278, Jun. 2010.
[41] J. Cai, Y. Wang, and Z. Qiao, "Multisymplectic preissman scheme for the time-domain Maxwell's equations," *J. Math. Phys.*, vol. 50, no. 3, pp. 033510-1–033510-18, 2009.
[42] W. Cai, Y. Wang, and Y. Song, "Numerical dispersion analysis of a multi-symplectic scheme for the three dimensional Maxwell's equations," *J. Comput. Phys.*, vol. 234, pp. 330–352, Feb. 2013.

Zhipeng Chen was born in Anqing, Anhui, China, in 1995. He received the B.S. degree from Hefei Normal University, China, Hefei, in 2018, and the M.S. degree from Anhui University, Hefei, in 2023, where he is currently pursuing the Ph.D. degree with the School of Electronic Information Engineering.

His research interests include computational electromagnetics, and finite-difference time-domain algorithms and antennas.

Linqing Li was born in Bozhou, Anhui, China, in 1995. He received the B.S. degree from Hefei Normal University, Hefei, China, in 2018, and the M.S. degree from Anhui University, Hefei, in 2021, where he is currently pursuing the Ph.D. degree with the School of Electronic Information Engineering.

His research interests include computational electromagnetics, and finite-difference time-domain algorithms and metamaterials.

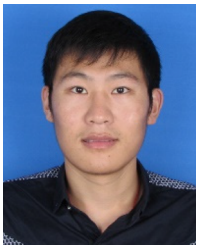

Chao Yang was born in Shandong, China, in 1991. He received the B.S. degree in applied physics from Xidian University, Xi'an, China, in 2014, and the Ph.D. degree in electronic science and technology from Zhejiang University, Hangzhou, China, in 2019.

He is currently an Assistant Researcher at the National Key Laboratory of Intense Pulsed Radiation Simulation and Effect, Xi'an. His research interests include computational electromagnetics, intense electromagnetic pulse environments, and electromagnetic scattering.

Wei E. I. Sha (Senior Member, IEEE) received the B.S. and Ph.D. degrees in electronic engineering from Anhui University, Hefei, China, in 2003 and 2008, respectively.

From July 2008 to July 2017, he was a Post-Doctoral Research Fellow and later a Research Assistant Professor with the Department of Electrical and Electronic Engineering, University of Hong Kong, Hong Kong. From March 2018 to March 2019, he held a Marie Skłodowska-Curie Individual Fellowship at University College London, London, U.K. In October 2017, he joined the College of Information Science and Electronic Engineering, Zhejiang University, Hangzhou, China, where he is currently a tenured Associate Professor. He has authored or co-authored over 200 peer-reviewed journal articles, 180 conference papers, 12 book chapters, and two books. His work has been cited over 12 804 times on Google Scholar, with an H-index of 59. His research focuses on theoretical and computational electromagnetics, including computational and applied electromagnetics, nonlinear and quantum electromagnetics, micro- and nano-optics, and multiphysics modeling.

Dr. Sha is a Life Member of OSA. He received multiple awards, including the ACES-China Electromagnetics Education Ambassador Award in 2024, the ACES Technical Achievement Award in 2022, and the PIERS Young Scientist Award in 2021. Nine of his students have won Best Student Paper Awards. He has reviewed more than 60 technical journals and served on the Technical Program Committees of over ten IEEE conferences. He is an Associate Editor of IEEE JOURNAL ON MULTISCALE AND MULTIPHYSICS COMPUTATIONAL TECHNIQUES, IEEE OPEN JOURNAL OF ANTENNAS AND PROPAGATION, IEEE ACCESS, and *Electromagnetic Science*.

Yingsong Li (Senior Member, IEEE) received the B.S. degree in electrical and information engineering and the M.S. degree in electromagnetic field and microwave technology from Harbin Engineering University, Harbin, China, in 2006 and 2011, respectively, and the joint Ph.D. degree from Kochi University of Technology (KUT), Kochi, Japan, and Harbin Engineering University (HEU), Harbin, in 2014.

He was a Professor with HEU from 2014 to 2022; a Visiting Scholar with the University of California at Davis, Davis, CA, USA, from March 2016 to March 2017; and a Visiting Professor with the University of York, York, U.K., in 2018, and Far Eastern Federal University (FEFU), Vladivostok, Russia, and KUT. He has been a Full Professor with the School of Electronic and Information Engineering, Anhui University, Hefei, China, since March 2022. He is currently a Visiting Professor with the School of Information, KUT, which he began in 2018. He is also a Post-Doctoral Fellow with the Key Laboratory of Microwave Remote Sensing, Chinese Academy of Sciences, Beijing, China, from 2016 to 2020. He has authored or co-authored approximately 300 journal articles and conference papers in various areas of electrical engineering. His research interests include remote sensing, underwater communications, signal processing, adaptive filters, metasurface designs, and microwave antennas.

Dr. Li is an Associate Editor of IEEE ACCESS, *Applied Computational Electromagnetics Society Journal* (ACES Journal), and *Alexandria Engineering Journal*.

Zhixiang Huang (Senior Member, IEEE) was born in Anhui, China, in 1979. He received the B.S. and Ph.D. degrees from Anhui University (AHU), Hefei, China, in 2002 and 2007, respectively.

Since 2008, he has been a Full Professor with the School of Electronic Information and Engineering, AHU. From September 2010 to September 2011, he was a Visiting Scholar with Iowa State University, Ames, IA, USA. From August 2013 to October 2013, he was a Visiting Professor with The University of Hong Kong, Hong Kong. From February 2014 to February 2015, he was a Visiting Professor with Beijing National Laboratory for Condensed Matter Physics, Institute of Physics, Chinese Academy of Sciences, Beijing, China. He has co-authored one monograph on the symplectic finite-difference time-domain method and two book chapters for CRC Press and Intech Publishers. He has co-authored 90 peer-reviewed journal articles included in the Web of Science Core Collection. His current research interests include time-domain numerical methods, metamaterials, and active antennas.

Dr. Huang was a recipient of the Second Prize of Science and Technology from Anhui Province Government, China, in 2015, and the National Science Foundation for Outstanding Young Scholar of China in 2017.

Xianliang Wu was born in Bozhou, China, in 1955. He received the B.S. degree in electronic engineering from Anhui University (AHU), Hefei, China, in 1982.

He is currently a Full Professor with the Department of Electronic Engineering and the Director of the Laboratory of Electromagnetic Field and Microwave Technology, AHU, and a Principal with Hefei Normal University, Hefei. He has authored or co-authored more than 70 articles and two books. His current research interests include electromagnetic field theory, electromagnetic scattering and inverse scattering, and wireless communication.

Prof. Wu is a Senior Member of Chinese Institute of Electronics. He was a recipient of the Ministry of Education Award for Science and Technology Progress and the Science and Technology Award, Anhui. He is an Associate Director of the Chinese Institute of Microwave Measurement.

Atef Z. Elsherbeni (Life Fellow, IEEE) received the Ph.D. degree in electrical engineering from Manitoba University, Winnipeg, MB, Canada, in 1987.

He started his engineering career as a part-time Software and System Design Engineer at the Automated Data System Center, Cairo, Egypt. He was a Professor of electrical engineering with the University of Mississippi, Oxford, MS, USA, where he became the Guest Dean for research and graduate programs at the School of Engineering. He has been a Dobelma Distinguished Professor and the Interim Department Head of the Department of Electrical Engineering and Computer Science and the EE Department Head, Colorado School of Mines, Golden, CO, USA.

Dr. Elsherbeni is a fellow of the Applied Computational Electromagnetics Society (ACES). He was selected as a Finland Distinguished Professor by the Academy of Finland and TEKES. He is the past Chair of the Engineering and Physics Division, Mississippi Academy of Science, and the Educational Activity Committee for the IEEE Region 3 Section, the General Chair of the APS-URSI Symposium, and the President of ACES. He is one of the IEEE Antennas and Propagation Society Distinguished Lecturers. He is the Editor-in-Chief of *Applied Computational Electromagnetics Society Journal* and a past Guest Editor of *Radio Science* journal.

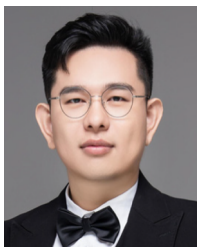

Kaikun Niu (Member, IEEE) was born in Anhui, China. He received the B.S. and Ph.D. degrees in electronic engineering from Anhui University (AHU), Hefei, China, in 2014 and 2019, respectively.

In 2017, he joined the Department of Electrical and Electronic Engineering, The University of Hong Kong (HKU), Hong Kong, as a Research Assistant. From 2018 to 2019, he was a Visiting Student with the King Abdullah University of Science and Technology, Thuwal, Saudi Arabia. From 2019 to 2020, he was a Post-Doctoral Research Fellow with the King Abdullah University of Science and Technology. He joined the School of Electronics and Information Engineering, AHU, in 2020, where he is currently an Associate Professor. He has authored or co-authored over 50 peer-reviewed journal articles and conference papers. He holds several granted Chinese patents. His current research interests include computational electromagnetics, electromagnetic compatibility, metamaterials, and nonlinear plasmonics.

Prof. Niu received the Young Scientist Award from the 14th International Symposium on Antennas, Propagation and EM Theory (ISAPE 2024) and the Young Scientist Honorable Mention Award at the 2025 International Applied Computational Electromagnetics Society Symposium (ACES-China 2025). In addition, he advised students on research that received Best Student Paper Awards at multiple international conferences, including the International Applied Computational Electromagnetics Society (ACES) Symposium, IEEE International Workshop on Electromagnetics (iWEM), and IEEE International Conference on Electronic Information and Communication Technology (ICEICT).